# DEVELOPMENT OF A DEFLECTION MEASUREMENT SYSTEM FOR THE HYBRID III SIX-YEAR OLD BIOFIDELIC ABDOMEN

By

Thomas Stanley Gregory V

Thesis submitted to the Faculty of the
Virginia Polytechnic Institute and State University
in partial fulfillment of the requirements for the degree of

MASTER OF SCIENCE

In

Biomedical Engineering

Warren N. Hardy, Chair
Stephen W. Rouhana
Stefan M. Duma

December 17, 2012

Blacksburg, Virginia

Keywords: hybrid, instrumentation, biofidelic, abdomen, deflection, measurement, dummy

**Development of a Deflection Measurement System for the Hybrid III Six-Year Old Biofidelic Abdomen**

Thomas Stanley Gregory V

**(Abstract)**

Despite advancements in automotive safety, motor vehicle collisions remain the leading cause of unintentional death for children ages 5 to 14. Enhancement of child occupant protection depends on the ability to accurately assess the effectiveness of restraint systems. Booster seat design and proper belt fit require evaluation using child anthropomorphic test devices, yet biofidelity of the abdomen and pelvis of the current anthropomorphic test device, the Hybrid III 6-year-old, needs improvement. Further, measurement of abdominal deflection is needed for quantification of the degree of submarining and associated potential injury risk.

A biofidelic abdomen for the Hybrid III 6-year-old dummy is being developed by the Ford Motor Company. A practical measurement system for the biofidelic abdominal insert has been developed and demonstrated for three dimensional determination of abdominal deflection. Quantification of insert deflection is achieved via differential signal measurement using electrodes mounted within a conductive medium. Signal amplitude is proportional to the distance between the electrodes. A microcontroller is used to calculate distances between ventral electrodes and a dorsal electrode in three dimensions.

This system has been calibrated statically, as well as evaluated dynamically. Its performance has also been demonstrated in a series of sled tests. Deflection measurements from the instrumented abdominal insert showed clear differences between two booster seat designs, yielding an average peak anterior to posterior displacement of the abdomen of $1.0 \pm 3.4$ mm and $31.2 \pm 7.2$ mm for the seats, respectively. Implementation of a 6-year-old abdominal insert with

he ability to evaluate submarining potential will likely advance the effectiveness of booster seat design and restraint performance, and help mitigate child occupant injury severity in automobile collisions.

**Acknowledgments**

I am very thankful for both the advice and encouragement from my advisor, Dr. Warren N. Hardy, who has introduced me into the field of impact biomechanics.

Meghan K. Howes for working with me to push this body of work into the eye of the public and for all the time and effort she put into this project with me.

Nathan Owen for his support and hard work.

I would like to thank Dr. Stephen W. Rouhana; someone who I feel has become both a mentor and a friend to me, for his support and guidance during the course of this project.

Dr. Stefan Duma for his wealth of knowledge and encouragement.

A special thank you goes to individuals at the National Highway Traffic Safety Administration (NHTSA) and the Vehicle Research & Test Center (VRTC) for their help in the evaluation of the system, especially Jason Stammen and Alena Hagedorn.

A thank you also goes out to Dr. John Bolte and Dr. Yun Seok Kang of the Injury Biomechanics Laboratory at The Ohio State University for their help and use of their facilities during the evaluation of the system.

I would also like to thank all my friends and family who helped to keep me encouraged and hard at work during this whole period of time.

## Table of Contents

## Listing of Figures and Tables

## Listing of Tables

## Listing of Equations

## Chapter 1: Introduction

Motor vehicle collisions are the leading cause of death for children 5 to 14 years of age. In 2009, 179,000 children ages 14 and younger sustained crash-induced injuries and accounted for 1,314 fatalities (Centers for Disease Prevention and Control, 2007; Traffic Safety Facts, 2009). Children in this age group are often times too large for child safety seats and too small for adult restraint systems. Despite advancements to infant and adult occupant protection systems, these children still remain at risk of injury, when not properly restrained in a belt-positioning booster seat, from abdominal interaction with the seatbelt or from partial restraint due to improper belt fit. Although 96 percent of parents think they have installed the car seat correctly, research has shown that 8 out of 10 have not (Putting Children First, 2000).

The most common injuries result from abdominal interaction with the seat belt, partial restraint, or complete ejection from the restraint system. To assess abdominal interaction with the restraint system, a biofidelic abdominal insert matching the force-deflection characteristics of the human abdomen is required. The reusable, rate-sensitive abdomen (RRSA) was designed for use within the HIII mid-sized male to provide a realistic response to automotive loading conditions during a frontal crash (Rouhana et al. 2001). To obtain a prototype of the pediatric abdomen, the RRSA was scaled in CAD. The shell thickness was determined using finite element modeling (Elhagediab et al. 2006), and the response of the scaled insert was compared to porcine belt-loading tests (Kent et al. 2006). A modified 6-year-old pelvis has been developed for the HIII dummy based on anthropometry data optimized from child medical images (Reed et al. 2009; Klinich et al. 2010). Pelvis bone structure was modified to match the position of the ASIS and pelvis flesh was altered to fit the new design. Compatibility with the concurrently developing abdominal insert was maintained. Sled testing with the modified pelvis indicated improvements compared to the standard pelvis including an appropriate submarining response and enhanced

sensitivity to belt placement. This should improve the ability of the dummy to discriminate between booster seat designs and potentially help all children that are still improperly restrained.

In order to fully assess abdominal interactions, a method of quantifying abdominal deflection of the HIII 6-year old insert is required. There were previous attempts at this; however they were unable to consistently measure deflection in 3 dimensions or were impractical. A practical measurement system for the HIII 6-year-old abdomen insert has been developed and demonstrated for three dimensional quantification of abdominal deflection. The system has been calibrated both statically and quasi-statically and has been evaluated using dynamic methods throughout various stages of the design process.

Implementation of the measurement system will enhance the assessment capability of the child dummies, especially with respect to measuring relative levels of submarining, leading to improved protection systems and child occupant injury mitigation.

*1.1 References*

Centers for Disease Control, Office of Statistics and Programming, National Center for Injury Prevention and Control, "10 Leading Causes of Injury Deaths by Age Group Highlighting Unintentional Injury Deaths, United States – 2007".

Elhagediab, AM., Hardy, WN., Rouhana, SW. Advancements in the rate-sensitive abdomen for the Hybrid III family of dummies, J. Biomechanics, 39 (2006).

Kent, R., Stacy, S., Kindig, M., Forman, J., Woods, W., Rouhana, SW., Higuchi, K., Tanji, H., Lawrence, SS., Arbogast, KB. Biomechanical Response of the Pediatric Abdomen, Part I: Development of an Experimental Model and Quantification of Structural Response to Dynamic Belt Loading. Stapp Car Crash J50. (2006)

Klinich, KD., Reed, MP., Manary, MA., Orton, NR. Development and Testing of a More Realistic Pelvis for the Hybrid III 6-Year-Old ATD. Traffic Injury Prevention 11 (2010): 606-612.

Putting Children First, 2000. NHTSA. **NTSB/SR-00/02**.

Reed, MP., Sochor, MM., Rupp, JD., Klinich, KD., Manary, MA. Anthropometric Specification of Child Crash Dummy Pelves through Statistical Analysis of Skeletal Geometry. J Biomechanics 42 (2009): 1143-1145.

Rouhana, SW., Elhagediab, AM., Walbridge, A., Hardy, WN., Schneider, LW. Development of a Reusable, Rate-Sensitive Abdomen for the Hybrid III Family of Dummies. Stapp Car Crash J 45 (2001).

Traffic Safety Facts, 2009. NHTSA. **US DOT HS 811 387**.

## Chapter 2: Background

### *2.1 Congressional Mandates*

The "Forgotten Children" have received congressional attention through the TREAD (Transportation Recall Enhancement, Accountability, and Documentation) Act of 2000 and Anton's Law of 2002. There are three major parts to the TREAD Act: vehicle manufacturers must report to the National Highway Traffic Safety Administration (NHTSA) when they conduct safety recalls in foreign countries; defect information must be reported to give consumers an early warning; and a manufacturer failing to comply with these rules when a safety-related defect has caused serious injury will be criminally liable. One specific feature of this act is the call for the review of the performance of child safety restraints. This includes a child restraint rating system, uniform restraint attachments, and improved safety standards (Public Law no. 106-414). Anton's Law was enacted to improve occupant safety for older children through the expansion of the Federal Motor Vehicle Safety Standards (FMVSS) to include children greater than 23 kg (H.R. 5504). Anton's law bears the name of a 4-year-old occupant who was fatally ejected from a vehicle during a rollover crash due to inadequate restraint by an adult three-point belt system. Anton's law mandates improvements in belt fit for children in booster seats, as well as lap-shoulder belt installation in all rear seats. The law states that children less than 145cm in stature and 36kg in weight should use a booster seat installed in the rear seat of a vehicle, which corresponds to an age of roughly 4 to 8 years. NHTSA recommends that these children should continue to use booster seats until they are either over 8 years of age or greater than 145 cm in stature. There are difficulties in making these recommendations, as age and height are not perfect predictors of booster seat belt fit. The law also calls for the development of a 10-year-old crash test dummy and associated pediatric injury criteria. FMVSS also lists test standards to be used for these dummies in a standard bench style seat specified in 49 US CFR Part 571.213.

*2.2 Injury Mechanisms*

A study of restrained child occupants with abdominal injury in frontal crashes showed that direct belt loading of the abdomen was the most common injury mechanism (Arbogast et al. 2007). For children ages 4 months to 17 years, 19% of the injuries to the gastrointestinal tract were attributed to interaction with the seatbelt (Canty et al. 1999). Belt compression injuries can result from submarining, in which the abdomen loads the lap belt directly as the anterior superior iliac spines (ASIS) of the pelvis slip under the belt. Small pelvis geometry puts children at a greater risk of submarining when using adult belts without booster seats. Further, child occupants who are too small for adult belts but are not seated on a booster seat are more likely to be out-of-position as those children tend to slide forward in the seat until the knee bends comfortably over the edge of the seat cushion (Klinich et al. 1994). This may position the lap belt over the abdomen with the potential for compression injuries in the event of a crash (Reed et al. 2009). Despite the injuries that may result from seatbelt usage, seatbelt use has been shown to significantly reduce traffic fatalities and serious injuries (Carpenter and Stehr, 2008).

*2.3 Pediatric ATDs*

A lack of both biomechanical and anthropometric data for children has impeded the development of child occupant safety assessment tools. Pediatric biomechanical data are limited as few pediatric cadaver studies have been published; totaling only 11 reported tests (Kallieris et al. 1976; Wismans et al. 1979; DeJeammes et al. 1984; Brun Cassan et al. 1993). Child volunteer data are restricted to non-injurious measures. Thus, the current child dummies and injury tolerance levels were derived from scaled adult response data and animal surrogate data (Pintar et al. 2000; Ching et al. 2001; Kent et al. 2006). Differences in material properties, error in

scaling and translating from surrogate anatomy yields uncertainty with regard to true child response.

Evaluation of booster seat effectiveness with child anthropomorphic test devices (ATDs) requires a biofidelic response of the abdomen and pelvis critical to the assessment of submarining and occupant-restraint interaction. However, the current Hybrid III (HIII) 6-year-old dummies lack biofidelity in the abdomen and pelvis, and are not instrumented to measure the injury risk of the abdomen. The standard abdomen is a vinyl-covered foam insert, and the pelvis geometry does not match the anthropometry of an average 6-year-old (Figure 2.1). Inaccurate ASIS geometry may unrealistic belt positioning relative to the ATD pelvis, resulting in inaccurate dummy kinematics with regard to submarining (Reed et al. 2009).

Figure 2.1: Regulatory abdomen (Elhagediab et al. 2007, Used under Fair Use, 2012)

Predictions of the 6-year-old dummy in sled tests with and without a booster seat contradicted injuries documented in the field (Sherwood et al. 2003). According to the sled tests, use of a booster seat resulted in injurious cervical spine loads while a three-point belt alone did not. Field data show cervical spine injuries to properly restrained children are rare. Further, in sled tests using only three-point restraints, the dummy did not submarine despite field data indicating submarining as a common injury mechanism for children restrained with three-point belts alone. Inaccuracies in the assessment of restraint safety for children can be attributed to the lack of biofidelity and the resulting inaccurate pelvis and abdomen interaction with a seatbelt exhibited by child dummies.

*2.4 HIII Pediatric ATD Advancements*

The reusable, rate-sensitive abdomen (RRSA) was designed for use within the HIII mid-sized male to provide a realistic response to automotive loading conditions (Rouhana et al. 2001). The insert consists of a silicone shell filled with fluid (silicone gel, water, and other fluids have been used) and was designed to match the biomechanical response corridors of rigid-bar (Cavanaugh et al. 1986; Hardy et al. 2001), seatbelt (Rouhana et al. 1989; Hardy et al. 2001) and airbag loading (Hardy et al. 2001). To obtain a prototype of the pediatric abdomen, the RRSA was scaled using computer aided design tools (CAD). The cavity that the abdomen would be housed in was digitized in order to develop boundary conditions for the insert, while the abdomen shell thickness was determined using finite element modeling (Elhagediab et al. 2007; Elhagediab et al. 2006). The response of the scaled insert was compared to the porcine belt-loading test of Kent et al. (2006).

A modified 6-year-old pelvis has been developed for the HIII dummy based on anthropometry data optimized from pediatric medical images (Reed et al. 2009). The medical images were used to generate finite element meshes of the skeletal geometry which were then aligned. A selected set of features were then quantified and the model was optimized into a single version using regression analysis of those features. Pelvis bone structure was modified to match the position of the ASIS and pelvis flesh was altered to fit the new dummy skeletal geometry. The pelvis maintained a similar outer appearance as the regulatory part, however pelvis flesh between where the the anterior inferior iliac spines (AIIS) would rest was removed in order to house the abdomen. There is also a well-defined iliac crest which leads into the ASIS and finally the AIIS. This leads to the appearance of a “hump” on either side of the pelvis, which will change how the pelvis interacts with the lap belt (Figure 2.2).

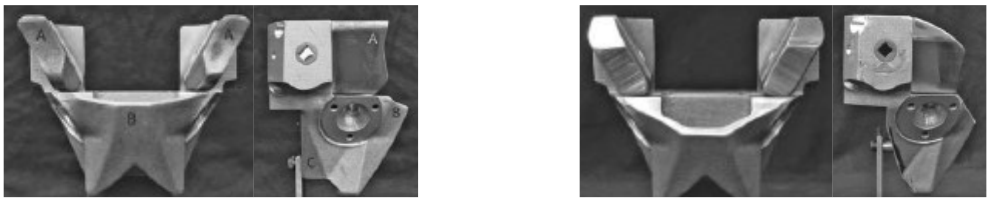

Figure 2.2: Regulatory (left) and modified pelvis (right) (Klinich et al. 2010, Used under Fair Use, 2012)

Compatibility with the concurrently developing abdominal insert was maintained, which includes the reduction of pelvis mass in order to compensate for increased abdominal mass. Sled testing with the modified pelvis indicated improvements when compared to the standard pelvis including an appropriate submarining response and enhanced sensitivity to belt placement, which was assessed in a series of sled tests using various belt anchoring locations (Klinich et al. 2010). A test was deemed to have an appropriate submarining response when a test in which the lap belt was initially placed on top of ASIS resulted in submarining. The combined abdomen and pelvis modifications also improve upon the ability of the dummy to discriminate between booster seat designs (Klinich et al. 2010).

*2.5 RRSA Deflection Measurement Systems*

There were several previous attempts to instrument the RRSA abdomen. This includes a 4-point Kelvin probe, ultrasound, 3D magnetic systems, force arrays (Rouhana et al. 2001), a light transmittance system based on Beer's law (Elhagediab et al. 2007) and an early system based on electrical conductance. These systems were either not practically realized (due to system size constraints, design issues, etc…) or experienced difficulties in 3D quantification of deflection. A deflection measurement system for the HIII 6-year-old abdomen insert has been developed and demonstrated for three dimensional quantification of abdominal deflection (Gregory et al. 2012). Implementation of the measurement system will enhance the assessment

capability of the child dummies, leading to improved protection systems and child occupant injury mitigation. Kent et al in 2008 proposed an injury criteria based on deflection, which reported deflection as a percent of total. To achieve the same resolution as this study, the abdominal deflection measurement system in the RRSA would have to sense on the order of 0.75 mm changes. The study also suggested that the system would be required to undergo at least ¾ of its total deflection in order to be used effectively. The resolution of the system presented by Gregory et al has not been quantified, however it has been designed to achieve sub-millimeter resolution as well as to response appropriately under extreme deflection.

*2.6 The Q Dummy Pediatric ATD*

Europe has adopted the Q dummy through its Child Advanced Safety Project for European Roads (CASPER) project (Lesire et al. 2012). The Q dummy contains an abdomen described as biofidelic and uses a set of twin pressure sensors for instrumentation. The biofidelity of the abdomen was assessed using a series of porcine tests from the literature (Rouhana et al. 1989). There has been a proposed set of injury criteria (based on pressure and rate of pressure change) made for the Q dummy system in Europe (Johannsen et al. 2012; Alonzo et al. 2006). The biofidelity and direct deflection measurement of the RRSA can potentially be used with a previously proposed deflection based injury criteria (Kent et al. 2008).

The Q dummy abdomen is instrumented with a set of pressure sensors (Alonzo et al. 2006) that give some localization information (left/right of centerline). This is done through the use of two contained pressure vessels within the insert. The pressure increases inside the abdomen when the abdomen is loaded. Since the sensors are both contained within fluid filled bladder, when the right sensor is loaded, the left sensor will also experience a change in pressure. An issue related to this fact is that any rib cage interaction will also appear as additional

abdominal loading and may give false positives. The Q dummy pressure sensors may be useful for the determination of injury versus no injury when the loading mode is known, such as in research environments. The system becomes at a disadvantage in production testing, where the loading mode may not appear as obvious. The current instrumentation and an updated version were tested and verified to correlate with injury during accident reconstructions using sled testing for AIS 3+ injuries (Beillas et al. 2012). Despite the ability to correlate with injuries in select testing modalities, the system may experience difficulties in localization of impact and determining the exact cause of injury. Since pressure is a result of many types of injury and abdominal interactions, the correlation is often times difficult to make. The RRSA abdomen deflection system is arguably a better choice in these situations, with its ability to localize impact by design, which will in turn assist in the identification and prediction of injury.

*2.7 References*


49 US CFR Part 571.213: Child Restraint Systems & Part 572: Subpart I – Six-Year-Old Child.

Alonzo, F., Bermond, F., Beillas, P. Child abdominal injuries in car restraint systems—An intra-abdominal pressure sensor for the Q-dummy family and proposed viscous injury criterion based on detailed accident analysis and their reconstructions. J. Biomechanics 39 (2006)

Anton's Law: Report (to accompany H.R. 5504), H.R. 5504, 1008-C, (2002).

Arbogast, KB., Kent, RW., Menon, RA., Ghati, YG., Durbin, DR., Rouhana, SW. Mechanisms of Abdominal Organ Injury in Seat Belt-Restrained Children. J of Trauma 62 (2007):1473-1480.

Beillas, P., Alonzo, F., Chevalier, MC., Lesire, P., Leopold, F., Trosseille, X., Johannsen, H. Abdominal Twin Pressure Sensors for the Assessment of Abdominal Injuries in Q Dummies: In-Dummy Evaluation and Performance in Accident Reconstructions. Stapp Car Crash J 56 (2012).

Brun Cassan, F., Page, M., Pincemaille, Y., Kallieris, D., Tarriere, C. Comparative Study of Restrained Child Dummies and Cadavers in Experimental Crashes. SAE Technical Paper Series 933105 (1993).

Canty, TG Sr., Canty, TG Jr., Brown, C. Injuries of the Gastrointestinal Tract From Blunt Trauma in Children. J of Trauma 46 (1999): 234-240.

Carpenter, CS., Stehr, M. The effects of mandatory seatbelt laws on seatbelt use, motor vehicle fatalities, and crash-related injuries among youths, Journal of Health Economics 27 (2008): 642-662.

Cavanaugh, JM., Nyquist, GW., Goldberg, SJ., King, AI. Lower Abdominal Tolerance and Response. SAE Technical Paper Series No 861878 (1986).

Ching, RP., Nuckley, DJ., Hertsted, SM., Eck, MP., Mann, FA., Sun, EA. Tensile Mechanics of the Developing Cervical Spine. Stapp Car Crash J 45 (2001).

DeJeammes, M., Tarriere, C., Thomas, C., Kallieris, D. Exploration of Biomechanical Data towards a Better Evaluation of Tolerance for Children Involved in Automotive Accidents. SAE Paper No. 840530 (1984).

Elhagediab, AM., Hardy, WN., Rouhana, SW. Advancements in the rate-sensitive abdomen for the Hybrid III family of dummies, J. Biomechanics, 39 (2006).

Elhagediab, AM., Hardy, WN., Rouhana, SW., Kent, RW., Arbogast, KB., Higuchi, K. Development of an instrumented rate-sensitive abdomen for the six year old Hybrid III dummy. JSAE Annual Congress Paper # 20075425 (2007)

Gregory, TS., Howes, MK., Rouhana, SW., Hardy, WN. Deflection Measurement System for the Hybrid III Six-Year-Old Biofidelic Abdomen. Biomed. Sci. Instrum. 48 (2012): 149-56

Hardy, WN., Schneider, LW., Rouhana, SW. Abdominal Impact Response to Rigid-Bar, Seatbelt, and Airbag Loading. Stapp Car Crash J 45 (2001).

Johannsen, H., Trosseille, X., Lesire, P., Beillas, P. Estimating Q-Dummy Injury Criteria Using the CASPER Project Results and Scaling Adult Reference Values. IRCOBI Conference (2012): 580-595.

Kallieris, D., Barz, J., Schmidt, G., Heess, G., Mattern, R. Comparison between Child Cadavers and Child Dummy by using Child Restraint Systems in Simulated Collisions. SAE Paper No.760815 (1976).

Kent, R., Stacey, S., Kindig, M., Forman, J., Woods, W., Rouhana, SW., Higuchi, K., Tanji, H., Lawrence, SS., Arbogast, KB. Biomechanical Response of the Pediatric Abdomen, Part I: Development of an Experimental Model and Quantification of Structural Response to Dynamic Belt Loading. Stapp Car Crash J 50 (2006).

Kent, R., Stacey, S., Kindig, M., Woods, W., Evans, J., Rouhana, SW., Higuchi, K., Tanji, H., Lawrence, SS., Arbogast, KB. Biomechanical Response of the Pediatric Abdomen, Part

II: Injuries and Their Correlation with Engineering Parameters. Stapp Car Crash J 50 (2008).

Klinich, KD., Pritz, HB., Beebe, MS., Welty, KE. Survey of Older Children in Automotive Restraints. SAE Paper No. 942222 (1994).

Klinich, KD., Reed, MP., Manary, MA., Orton, NR. Development and Testing of a More Realistic Pelvis for the Hybrid III 6-Year-Old ATD. Traffic Injury Prevention 11 (2010): 606-612.

Lesire, P., Johannsen, H., Willinger, R., Longton, A. CASPER – Improvement of child safety in cars. Procedia: Social and Behavioral Sciences 48 (2012): 2654-2663.

Pintar, FA., Mayer, RG., Yoganandan, N., Sun, E. Child Neck Strength Characterizations Using an Animal Model. Stapp Car Crash J 44 (2000).

"Public Law 106-414: Transportation Recall Enhancement, Accountability, and Documentation (TREAD) Act." (114 Stat. 1800., Date: 2000).

Reed, MP., Sochor, MM., Rupp, JD., Klinich, KD., Manary, MA. Anthropometric Specification of Child Crash Dummy Pelves through Statistical Analysis of Skeletal Geometry. J Biomechanics 42 (2009): 1143-1145.

Reed, MP., Ebert, SM., Sherwood, CP., Klinich, KD., Manary, MA. Evaluation of the Static Belt Fit Provided by Belt-Positioning Booster Seats. Accident Analysis and Prevention 41 (2009): 598-607.

Rouhana, SW., Viano, DC., Jedrzejczak, EA., McCleary, JD. Assessing Submarining and Abdominal Injury Risk in the Hybrid III Family of Dummies. Stapp Car Crash J 33 (1989).

Rouhana, SW., Elhagediab, AM., Walbridge, A., Hardy, WN., Schneider, LW. Development of a Reusable, Rate-Sensitive Abdomen for the Hybrid III Family of Dummies. Stapp Car Crash J 45 (2001).

Wismans, J., Maltha, J., Melvin, JW., Stalnaker, RL. Child Restraint Evaluation by Experimental and Mathematical Simulation. SAE Paper No.791017 (1979).

## Chapter 3: Design of 3-Dimensional Deflection Measurement System for Hybrid III Six-Year Old Biofidelic Abdomen

### *3.1 Introduction*

An instrumented biofidelic abdominal insert for the HIII 6-year-old dummy has been developed in conjunction with the Ford Motor Company. Early methods of instrumenting the abdominal insert included light transmittance, resistive gel, and Kelvin probe based designs, some of which were not fully developed. Those early prototypes that were deemed realistic were limited in their ability to quantify deflection, particularly in three dimensions. Those limitations were addressed in the development of the abdominal deflection measurement system described below. Figure 3.1 shows a block diagram for one channel of the entire system.

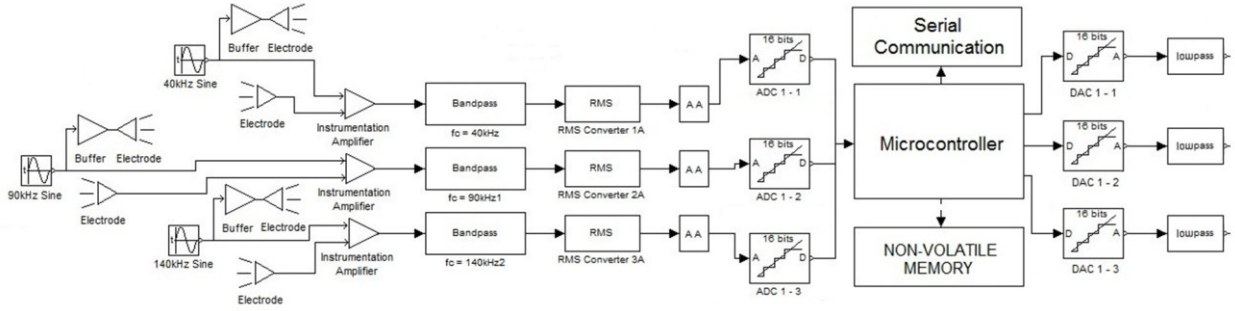


**Figure 3.1:** Single channel system block diagram

### *3.2 Analog System Design*

Real-time quantification of abdominal insert deflection is achieved via differential signal measurement using electrodes mounted within a conductive medium. The silicone abdominal shell is filled with a low-conductivity (160 μS/cm) saline solution, which provides a constant level of electrical resistivity.

Ten stainless steel electrodes are mounted in the fluid-filled insert; six measurement electrodes are mounted to the inner ventral surface, one electrode is mounted to the inner surface

of the dorsal aspect of the shell, and three fixed electrodes form a reference plane in the inferior posterior portion of the insert. These electrodes are then strain-relieved in the abdomen and ported out through the back of the abdomen insert (Figure 3.2).

Figure 3.2: Photo of an electrode (left), the reference plate (center), and the cable port (right)

The final prototype contained six ventral electrodes (Figure 3.3), while an earlier version contained only 3. The measurement electrodes are mounted to the shell at locations where the quantification of deflection is desired for the assessment of belt loading.


**Figure 3.3:** Instrumented biofidelic abdominal insert mounted on the HIII 6yo modified pelvis.

Three different carrier sinusoidal waveforms (40, 90, 140 kHz) are applied to each fixed electrode in the reference plane with respect to system ground. The potential difference between the fixed electrodes and the electrodes on the inner surface is measured using high input impedance circuitry (Figure 3.4). The same circuitry is used for each measurement.

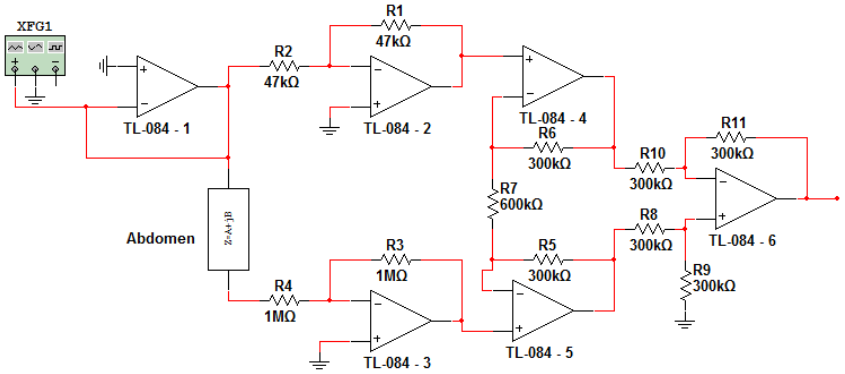


Figure 3.4: Input Circuitry

As the distance between the electrodes is varied, amplitude modulation of the sinusoidal carrier waveform that is proportional to the level of displacement occurs due to the change in resistance. The voltage output tends to increase as the displacement increases.

Each potential difference measurement contains an amplitude-modulated mixed-frequency AC signal. The signal is separated according to its constituent frequencies using three $4^{th}$ order bandpass filters (Figure 3.1 and 3.6) having a Butterworth profile (Figure 3.5). The filters each contain a passband less than 10 kHz, and ~ 45 kHz on either side of the center frequency, a signal attenuation of no less than 50dB is observed. Each filter is composed of four $2^{nd}$ order filter stages, with the final stage applying a gain of 3.

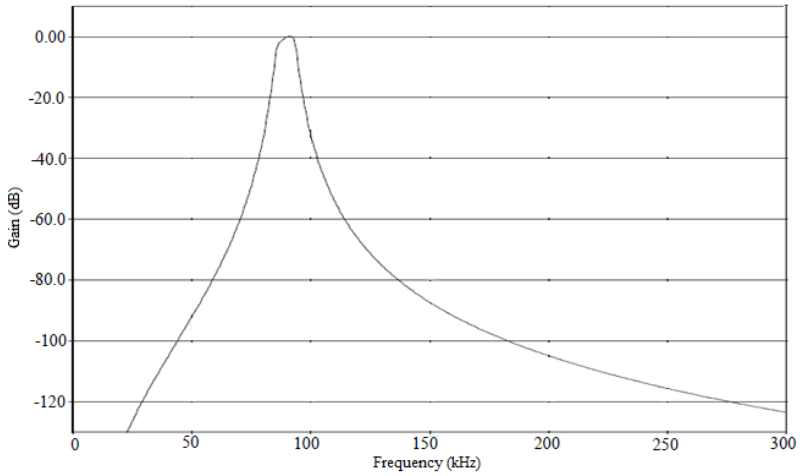


**Figure 3.5:** 90kHz bandpass filter frequency response, as designed.

After constituent signal separation, the true root-mean-square value of each sinusoidal waveform is calculated and converted into a proportional DC voltage. A full active rectifier circuit is used to convert the signal to a unipolar current. The active rectifier is used in order to reduce cost of the device. This allows for a single quadrant multiplier to be used (positive inputs and outputs). The current is sent through a multiplier/divider circuit which squares the input and divides it by the output. The output of the divider is sent through a low pass filter with an averaging capacitor to set signal averaging time. The low pass filter averages the input signal, which produces an output that can be reduced to form the root-mean-square of the input sinusoidal waveform. The RMS to DC conversion is performed using an AD637 (Analog Devices, Norwood, Ma). A gain of 5 is then applied to the signal before it is passed to the digital system (Figure 3.6).

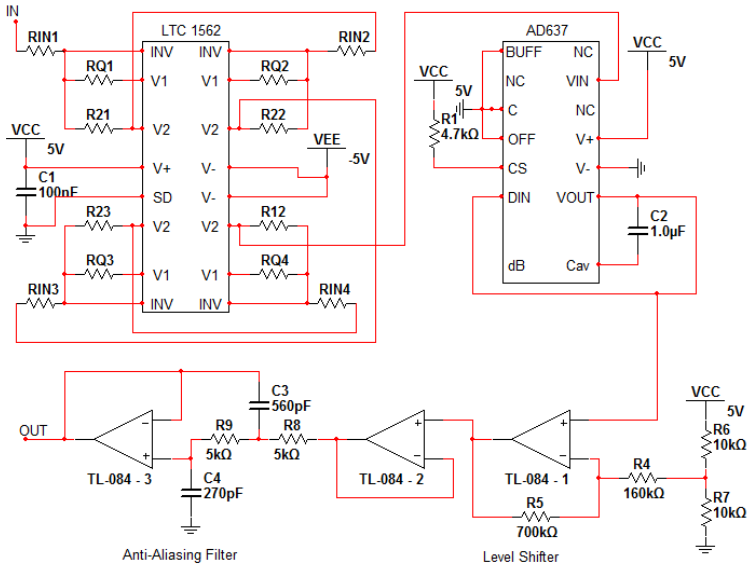


Figure 3.6: Signal Conditioning Circuitry

The resistances used for the LTC-1562 IC are different for each frequency used in the abdomen circuitry and can be viewed in Table 3.1.

Table 3.1: Filter Resistances

| | 40 kHz | 90 kHz | 140 kHz |
|---|---|---|---|
| R2 (kΩ) | 62.5 | 12.3 | 5.1 |
| RQ1(kΩ) | 249 | 110 | 71.5 |
| RQ2 (kΩ) | 499 | 220 | 107 |
| RQ3 (kΩ) | 360 | 220 | 107 |
| RQ4 (kΩ) | 249 | 110 | 71.5 |
| RIN1 (kΩ) | 249 | 110 | 71.5 |
| RIN2 (kΩ) | 298 | 220 | 169 |
| RIN3 (kΩ) | 298 | 220 | 169 |
| RIN4 (kΩ) | 62.5 | 44 | 33 |

*3.3 Digital System Design*

The signal is passed to the digital board through a section of anti-aliasing filters (Figure 3.6) implemented with a Butterworth frequency response and a cutoff of 8 kHz using a TL-084 integrated circuit (Texas Instruments, Dallas, Tx). This is to prevent signal artifacts that could occur during digitization. The digitization is performed at a rate of 20ksps using three eight-channel, 16-bit analog-to-digital converter chips (AD7606, Analog Devices, Norwood, MA). The analog-to-digital converters have high input impedances which eliminates the need for driver amplifiers. An internally generated conversion clock sets the signal sampling time to 4μs for all channels. The converter uses successive approximation style architecture. This style compares the input voltage sampled using track-and-hold amplifiers to an internally generated voltage. The internally generated voltage is incremented using a 16-bit register attached to a digital-to-analog converter. The converter cycles bit states from low to high through the most significant to the least significant bit, leaving the bit high only if the comparator indicates that its corresponding voltage level has not surpassed the input voltage at that time point. The resulting data is then sent to a tri-state output bus to wait until it has been signaled to appear on the external bus. The third state of the bus, after high (+5V) and low (0V), is a high impedance mode

which allows each converter to be connected together and read using a single microcontroller. The trace lengths of the bus were sized to ensure that all the bits from the converter arrive at the microcontroller at the same time.

A PIC32MX360F512L (Microchip Technology Inc, Chandler, Az) was utilized as the microcontroller due to its specialized architecture. The device has several dedicated hardware ports for inter-circuit communications (rather than software simulation), as well as a single cycle multiply unit. This allows for the device to handle high-speed calculations and communications. The device also employs a type of pipelining architecture that allows for necessary operations with a high latency to have an increased throughput. The device consists of a MIPS32 core, which is a widely-used 32 bit architecture with a RISC instruction set.

The microcontroller is employed to calculate three-dimensional displacement of the six ventral electrodes using the sampled signals. The code for the microcontroller was written in C and can be seen in Appendix B. Figure 3.7 shows the organizational flow chart for the microcontroller program.

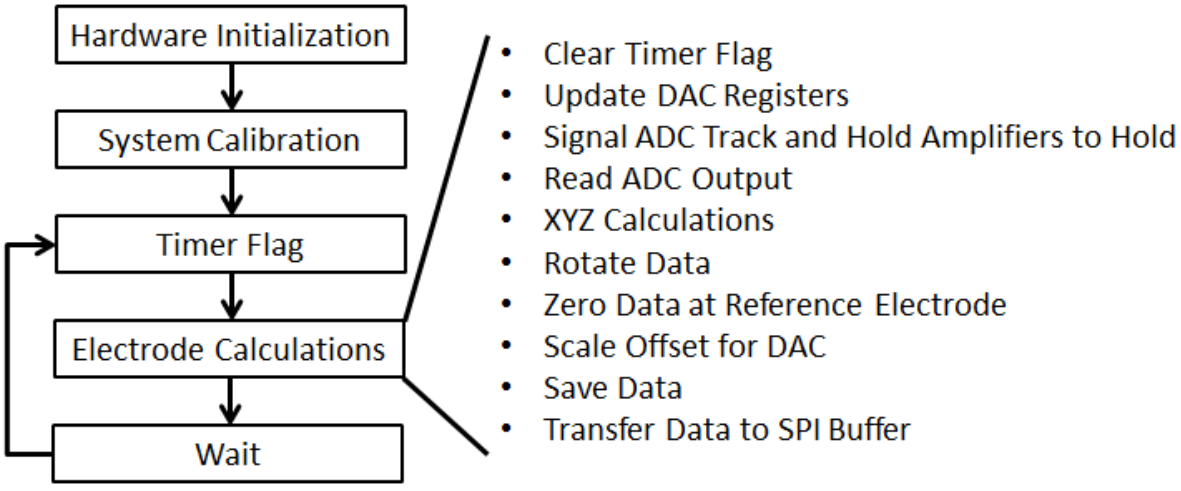


**Figure 3.7:** Microcontroller program flow chart

A method of trilateration is applied to perform these calculations based on the distances between the electrodes on the reference plane and those attached to the shell. Electrode placement was selected to simplify calculations, with all three reference electrodes located in the Z-plane and two of the reference electrodes located in the X-plane. Trilateration works by envisioning each measured distance as the radius of a sphere, r, with one of the reference electrodes at the center (Manolakis, 1996). The point of interest is located at the sole intersection of all three spheres, which can be calculated using a system of three equations with three unknowns. Solving this system yields the three-dimensional displacement of the point of interest (Equations 3.1, 3.2, 3.3). The coordinates of the reference points must be defined as: (0,0,0); (*d*,0,0); (*i*,*j*,*0*). These equations are further simplified when *i* and *j* are equal.

$$X = \frac{r_1^2 - r_2^2}{2d} + \frac{d}{2} \qquad \text{(eq. 3.1)}$$

$$Y = \frac{r_1^2 - r_3^2 + i^2 + j^2}{2j} - \frac{i}{j}X \qquad \text{(eq. 3.2)}$$

$$Z = abs(\sqrt{r_1^2 - x^2 - y^2}) \qquad \text{(eq. 3.3)}$$

The calculated displacement is then transformed into the dummy coordinate system (Figure 3.8) from the coordinate system of the reference plane using a series of rotation matrices (Equations 3.4, 3.5).

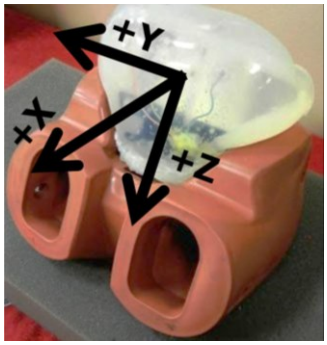


Figure 3.8: Dummy Coordinate System

The first matrix aligns the abdomen coordinate system near the dummy coordinate system, while the second matrix is used to account for the angle that the electrode reference plane is mounted on. The data is then translated 25.4 mm in the –Z direction and in the +X direction.

$$\begin{bmatrix} x' \\ y' \\ z' \end{bmatrix} = \begin{bmatrix} 1 & 0 & 0 \\ 0 & 0 & 1 \\ 0 & 1 & 0 \end{bmatrix} \begin{bmatrix} x \\ y \\ z \end{bmatrix} \qquad \text{(eq. 3.4)}$$

$$\begin{bmatrix} x'' \\ y'' \\ z'' \end{bmatrix} = \begin{bmatrix} 0 & \cos(20^o) & -\sin(20^o) \\ 1 & 0 & 0 \\ 0 & -\sin(20^o) & -\cos(20^o) \end{bmatrix} \begin{bmatrix} x' \\ y' \\ z' \end{bmatrix} \qquad \text{(eq. 3.5)}$$

Displacement values are sent to digital-to-analog converters (AD-5066, Analog Devices, Norwood, MA) in real time so that they may be recorded from single-ended outputs by traditional data acquisition equipment. The digital-to-analog converters employ 16-bit R-2R ladder architecture in order to accomplish this.

Since the output only occurs at discrete levels a passive, single pole low pass filter is employed as a quantization filter using a cutoff of 8 kHz. This removes the step-like appearance of the signal. In order to make the system more user friendly, a level shifting amplifier is added as the final stage. This amplifier allows the system to generate positive and negative voltage swings using a single supply digital-to-analog converter. The circuit diagram for the digital board can be seen in Figure 3.9. The schematic includes power decoupling and biasing. The anti-aliasing filters can be viewed in Figure 3.6 with the signal conditioning circuitry.

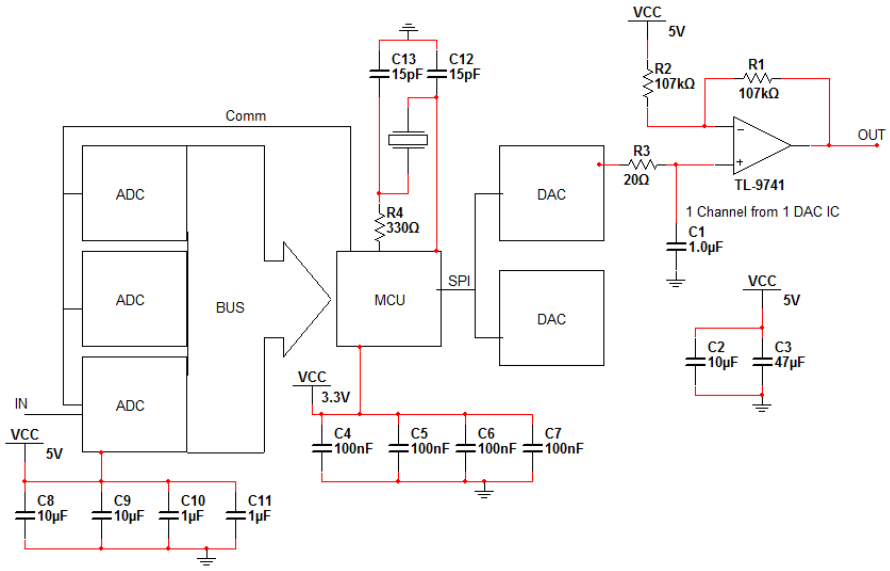


Figure 3.9: Digital System Schematic

These positive and negative voltage swings will be proportional to positive and negative electrode displacements. The system is able to auto-zero these outputs on power-up. A hardware switch can also be utilized to perform this function.

The single-ended outputs can be interfaced to traditional data acquisition. In an effort to miniaturize the system, the circuits were manually routed, each with four layers and dedicated power, ground, and signal planes to reduce noise in order to produce printed circuit boards. The completed system consists of the digital control printed circuit board in a stacked configuration with two analog signal processing printed circuit boards and can be mounted in a location near to the ATD (Figure 3.10). A method of reflow soldering was used to populate the boards. The system is mounted within a ventilated enclosure that can be mounted directly to test fixtures using a 4” x 4” bolt pattern (clearance holes for 1/2”-13 bolts).

**Figure 3.10:** Digital (left), analog (center), and full enclosure (right).

*3.4 References*

Manolakis, DE. Efficient solution and performance analysis of 3D position estimation by trilateration. IEEE Transactions on Aerospace and Electronic Systems. 32 (1996): 1239-49

## Chapter 4: Static Calibration and Dynamic System Evaluation

### *4.1 Static Calibration*

A Materials Testing Machine (MTS, Eden Prairie, MN) was used to provide anterior-posterior compression directly to the abdominal insert using a seatbelt yoke with an 18 inch width (Figure 4.1). The thorax-lumbar interface plate and a custom-built lumbar spine surrogate were used in conjunction with the pelvis in order to apply boundary conditions to the test area. The seatbelt was initially positioned superior to dummy pelvis anterior superior iliac spine. This was implemented to simulate submarining of the dummy abdomen and allowed the electrodes to be displaced in other directions. The electrode displacements were recorded at a sampling rate of 20 kHz using a TDAS Pro data acquisition system (Diversified Technical Systems, Seal Beach, California).

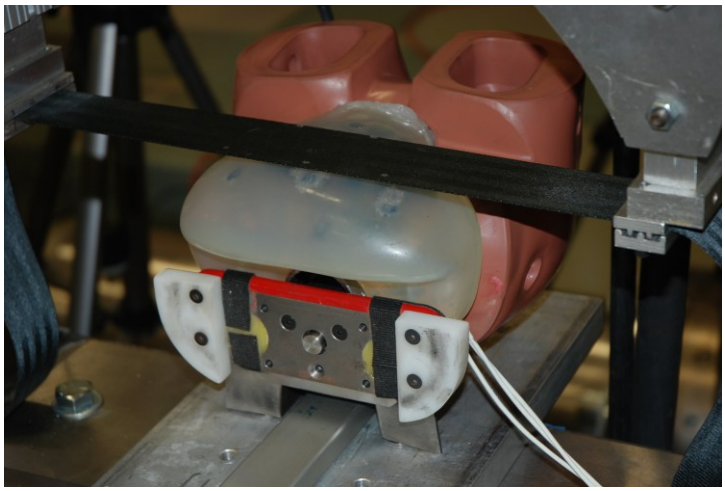

**Figure 4.1:** Static seatbelt loading apparatus

The yoke was displaced incrementally from 0 to 50.8 mm (2”). The displacement measured by the electrodes did not equal the applied displacement of the yoke because the load was applied using flexible seatbelt webbing. In order to find an initial measure of electrode position as well as incremental displacement, and to address the inaccurate displacement

readings of the MTS, a FARO arm was used. At each level of displacement, the external and internal measurements were recorded using the FARO arm and the deflection measurement system, respectively. The relationship between the raw output of the FARO arm and abdomen electrodes in the X, Y, and Z directions are illustrated in Figures 4.2, 4.3, and 4.4, respectively. The error is then minimized by updating the previous sensitivities with the new values from this calibration, based on relationships determined through this process. The electrodes are numbered as previously described in Figure 4.1.

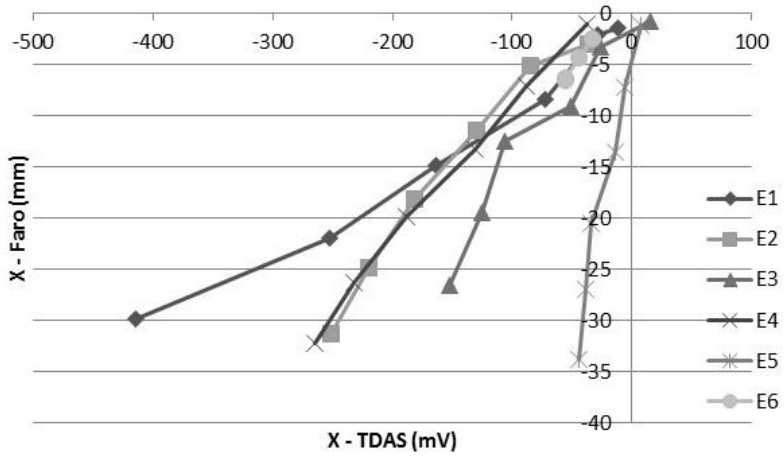


**Figure 4.2:** Comparison of abdomen output and measured displacement in the X direction

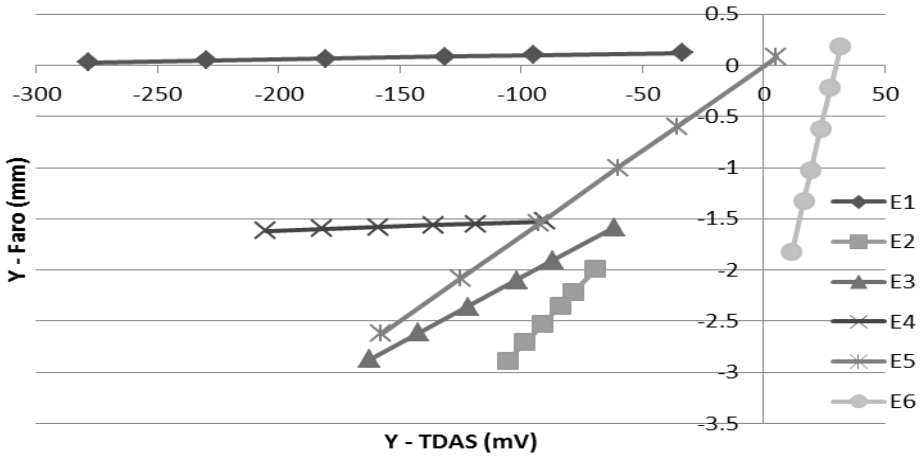


**Figure 4.3:** Comparison of abdomen output and measured displacement in the Y direction

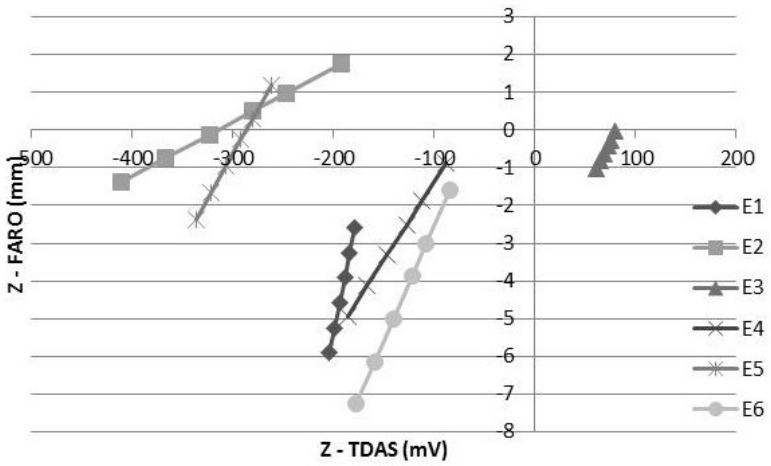


**Figure 4.4:** Comparison of abdomen output and measured displacement in the Z direction

The sensitivity was calculated through a custom Matlab (MathWorks, Natick, Ma) library, which read in the data collected during calibration and determined sensitivity values (mV/EU) for each system output. The test data was filtered at channel frequency class (CFC) 1000 Hz. This allows any user of the system to easily recalibrate it using raw data.

Table 4.1: Calibration Linearity

| | Slope (mm/mV) | | | Correlation | | |
|---|---|---|---|---|---|---|
| | X | Y | Z | X | Y | Z |
| 1 | 0.072 | 0.001 | 0.130 | 0.98 | 0.99 | 0.99 |
| 2 | 0.134 | 0.025 | 0.014 | 0.98 | 0.99 | 0.99 |
| 3 | 0.147 | 0.013 | 0.052 | 0.96 | 0.99 | 0.99 |
| 4 | 0.134 | 0.001 | 0.042 | 0.99 | 0.99 | 0.99 |
| 5 | 0.589 | 0.017 | 0.048 | 0.98 | 0.99 | 0.99 |
| 6 | 0.172 | 0.101 | 0.061 | 0.99 | 0.99 | 0.99 |

*4.2 Dynamic Testing Methods*

The abdomen surface was impacted using a 5.9 kg (13 lbs.) pendulum at a speed of 3 m/s. The impact surface was a 25.4 mm (1") diameter, 305 mm (12") long rigid bar. The impact speed was chosen to achieve between 25.4 and 50.8 mm (1" to 2") of anterior-posterior deflection.

The ATD was in a seated free-back position which allowed for posterior movement during impact. A load cell was mounted within the pendulum. The pendulum and lumbar spine were tracked visually using high-speed cameras to quantify deflection. A Phantom V9.1 (Vision Research, Wayne, NJ) camera was used to record the impacts at 1000 Hz with a 990 μs exposure and a 1440 x 720 pixel resolution. The pendulum was tracked using points on the rigid bar and on the shaft, while the lumbar spine was tracked using a mount with three visual markers. The tilt of the pendulum was not accounted for; however the spine markers were used to account for spine bending. Point of contact was determined to be one frame prior to observed initial deflection of the abdomen. There are issues that may arise with this approach, instead of an actual contact switch. The distance between two points on the pendulum was measured throughout each test in order to get a sense of error that occurred across the viewing area. The points were approximately 270 mm apart, and the standard deviation measured across all tests was 3 mm. Three tests were performed with the purpose of comparing deflection across the face of the abdomen with measured peak deflection calculated from high-speed video. The height of the pendulum was adjusted such that it would primarily interact with the top row of electrodes. The abdomen data for this test series was filtered using at CFC 600 Hz.

*4.3 Dynamic Testing Results*

The mean displacement ± 1 standard deviation for each test was calculated for the second test series (Figure 4.9 – 4.14). The mean maximum speed of the pendulum was recorded to be 3.0 ± 0.08 m/s. This was calculated through measuring the displacement over time 5 frames before initial contact with the abdomen. The displacement measured using high-speed camera data in the X direction was -30.09 mm ± 5.05 mm. This is higher than the recorded maximum displacement using the deflection measurement system. This is most likely due to the fact that

the displacement in the Z direction was found to be -16.65 mm ± 3.90 mm, which would indicate that the electrodes moved superiorly with the pendulum. Additional errors may be associated with the fact that the pendulum tilt was not accounted for. A correction was performed on each frame to rotate the tracked spine point based on the rotation of a vector described by the middle and top spine markers. The maximum deflection was observed to occur above the top row of electrodes, which was confirmed qualitatively from video by comparing the location of the pendulum with respect to the pelvis and the location of the abdomen deflection electrodes with the pelvis when mounted statically (Figure 4.5). Further confirmation of this would require altering the testing configuration.

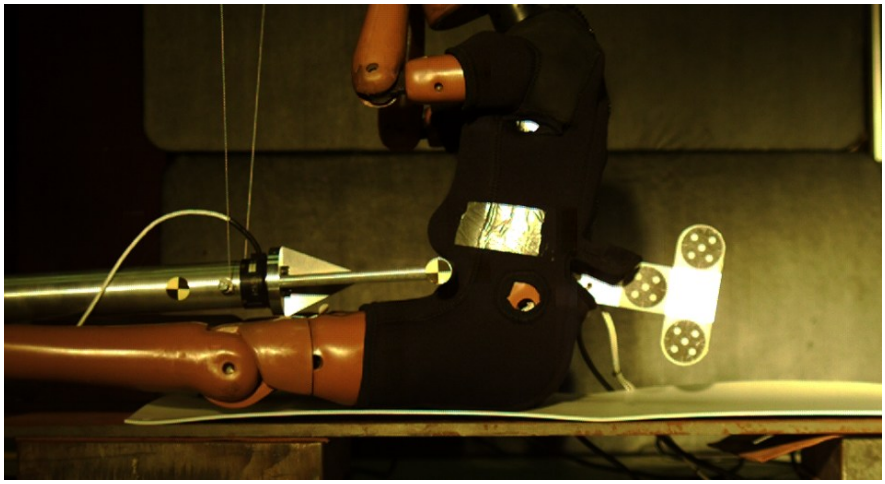

**Figure 4.5:** View of test-setup for the second test in the series.

The point of impact can be observed to be above the top of the pelvis through the dummy suit. This corresponds to the approximately at the same location as the top row of electrodes, with the center electrode being slightly above the pendulum. In Figure 4.5, the top of the abdomen can be seen curling around the pendulum where the center electrode is located.

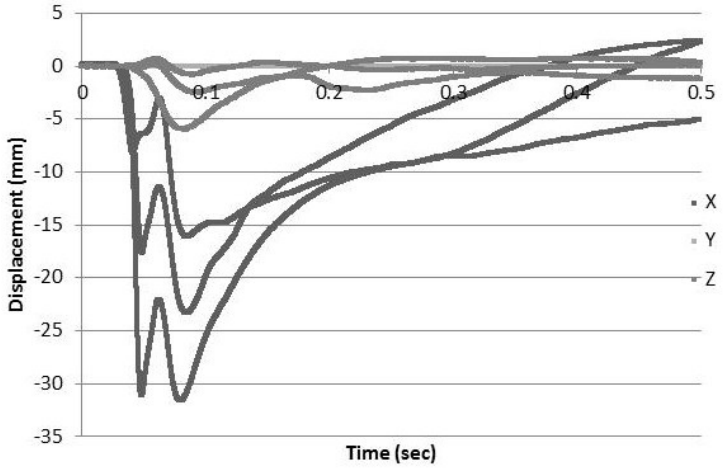


**Figure 4.6:** Average displacement in the X, Y, and Z directions for the top left electrode (E1).

The top left electrode (Figure 4.6) exhibits a bimodal response which can be observed during high-speed video. The hypothesis of this paper is that the bimodal response is most likely due to the left and right (Figure 4.8) electrodes being loading indirectly through the direct loading of the center electrode (Figure 4.7) by the pendulum. This would occur upon the direct loading of the left and right electrodes after this point. This effect is also visible in the lower electrodes to a lesser extent.

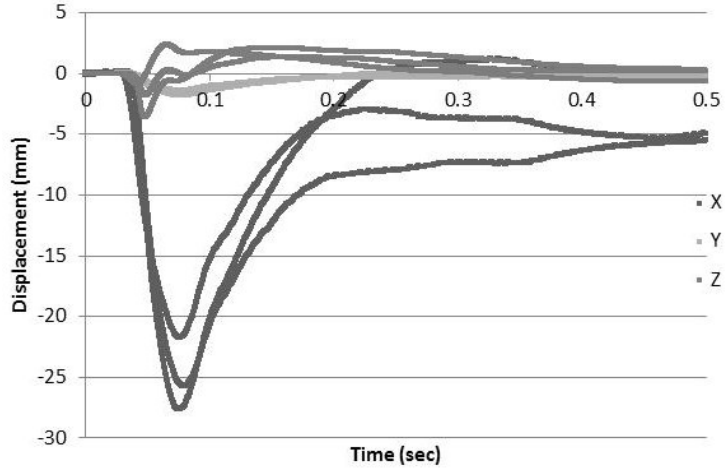


**Figure 4.7:** Average displacement in the X, Y, and Z directions for the top center electrode (E2).

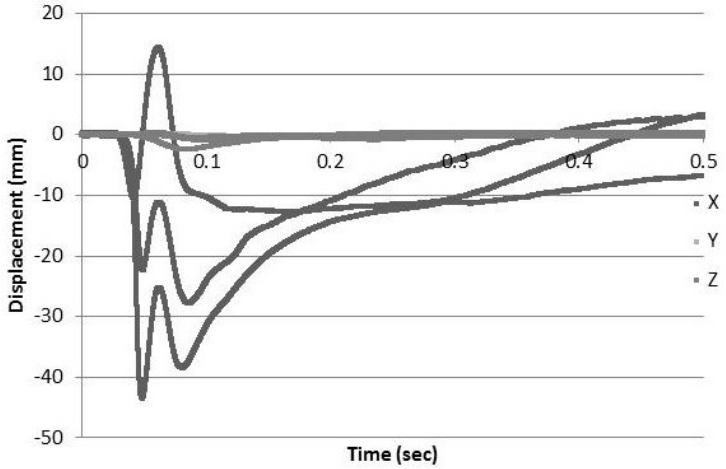


**Figure 4.8:** Average displacement in the X, Y, and Z directions for the top right electrode (E3).

It can be observed that the displacement of the electrodes on the top row is a similar order of magnitude. The difference across the row is caused by the 5 mm superior placement of the top center electrode with respect to the left and right electrodes, which was measured directly using a caliper. There also is a slight difference in the placement of the left and right electrodes in the Z directions. These differences lead to the non-direct interaction of the pendulum with the electrodes.

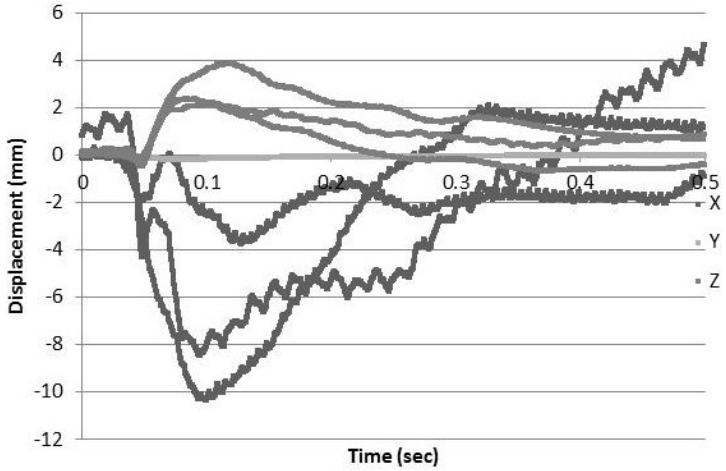


**Figure 4.9:** Average displacement in the X, Y, and Z directions for the middle left electrode (E4).

There is a larger level of noise present in the signals coming from the middle left electrode, particularly in the X direction (Figure 4.9). This was found to be an issue with the

cable shielding, however to maintain consistency in the data set, the CFC was not changed to reduce the noise further. The shielding was found to have a ground connection on either side of the connector, which allows induced current to flow across the cable and subject the signal to greater levels of interference.

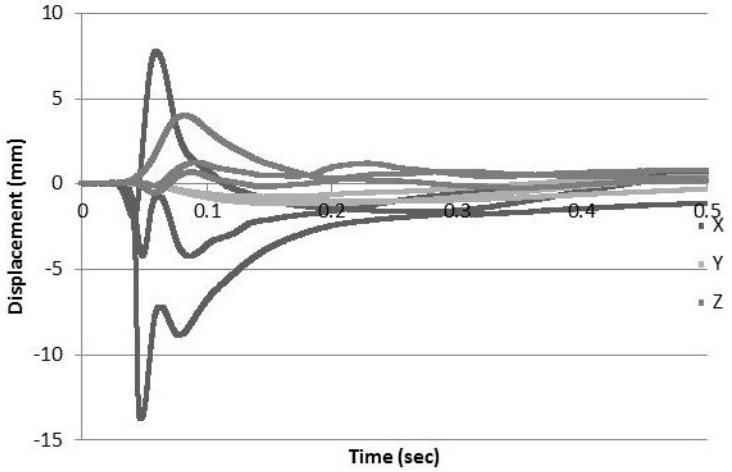


**Figure 4.10:** Average displacement in the X, Y, and Z directions for the middle right electrode (E5).

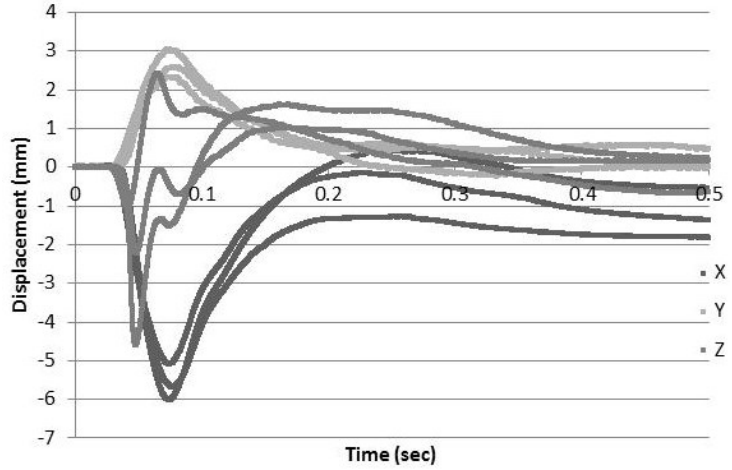


**Figure 4.11:** Average displacement in the X, Y, and Z directions for the bottom electrode (E6).

The displacement is clearly seen decreasing as the distance from the electrode to the impact location increases. From the deflection curve in the X-direction for electrode 2 (top center) and the visually tracked displacement curve, an assessment of the system performance can be made (Figure 4.12).

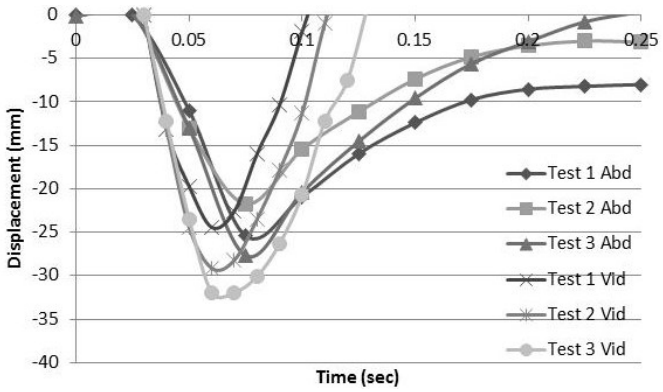


**Figure 4.12:** Measured +X deflection for visually tracked and internally recorded data (E2)

It was previously shown that the center electrode experienced a lower level of deflection than the left and right electrodes on the top row. If the tracked data is compared to either the left or right electrode on the top row, then the data tends to agree in magnitude on a greater level (Figure 4.13).

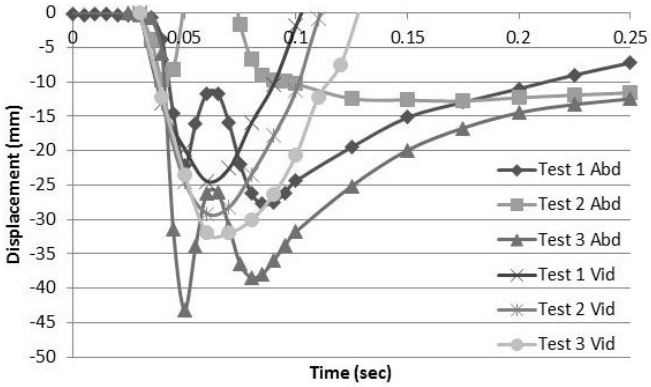


**Figure 4.13:** Measured +X deflection for visually tracked and internally recorded data (E3).

If the bimodal response seen in the right electrode is ignored for the time being, then it becomes apparent that the magnitudes tend to agree.

A $6^{th}$ order polynomial was fit to each paired video and abdomen center electrode data set until 0.1 seconds into the test. For tests 1 to 3, the regression coefficient was calculated to be 0.84, 0.84, and 0.90, respectively. This gives the sense that the curves for each test tend to agree, however it is not a statistical test.

*4.4 Discussion*

From the appearances of the curves obtained from the abdomen deflection system during the pendulum impacts, a few conclusions can be drawn.

The first conclusion is drawn from the differences in displacement between the 2nd (center) electrode and the left and right (1st and 3rd) electrodes. The pendulum impacted the abdomen at a slightly upward angle going into this row of electrodes. The 1st and 3rd electrodes being impacted directly, while the slightly superior 2nd electrode being impacted by the top of the bar. This causes the 2nd electrode to wrap around the impact surface and not experience the full level of displacement.

The second fact that is made apparent is the variation in displacement (bimodal response) during the loading phase of the event that is seen in the 1st and 3rd electrodes. This variation can also be seen to a lesser extent in the 4th and 5th electrodes. This occurs at the point when the center electrode has been displaced by about 5mm. From the measurement of the abdominal insert, it can be seen that the original location of the center electrode is about 5mm farther away from the dorsal electrode in the X direction than the left and right electrodes. This would suggest that the loading of the center electrode before the bar comes into contact with the left and right electrode causes them to be displaced at a slightly lower rate. The hypothesis of this paper is that the bimodal response is caused by the initial deflection on the center electrode causing indirect deflection in the left and right electrodes to a lesser extent. The pendulum then comes into contact with the rest of the abdomen and the left and right electrodes are then deflected directly. The bimodal response caused by the pendulum impacting different surfaces of the abdomen at different points in time was confirmed upon further video inspection. The positioning of the dummy may also further exaggerate this effect. The size of the test area restricts the positioning

of the dummy, and can lead to slight misalignments of the dummy coordinate system with respect to the laboratory coordinate system. This misalignment will lead to the pendulum impacting the surface of the abdomen unevenly; however the differences observed by the measurement system are only on the order of a few millimeters.

It can also be noted that that the recorded deflection for each electrode does not return to the pretest values after the impact. Considering the magnitude of these numbers and the type of impact, it is reasonable to assume that post-test the final dummy position is not the same as the initial dummy position. This difference means that the thorax of the dummy will tend to rest differently on the superior surface of the abdomen and will prevent the electrodes from returning to their initial positions.

There was little movement recorded in the $4^{th}$, $5^{th}$ and $6^{th}$ electrodes compared to the $1^{st}$, $2^{nd}$, and $3^{rd}$ electrodes during this test series. This was to be expected due to the point of impact observed during the high-speed video. The signal to noise ratio of the $4^{th}$ electrode seemed to be abnormally low during this test series; however its data does tend to agree with the $5^{th}$ electrode. The data tends to correspond with both the visually tracked data and what is expected based on the type of impact.

## Appendix A: Comparison of Ability of Instrumented Biofidelic Abdominal Insert and Modified Pelvis to Regulatory Hybrid III Dummy to Evaluate Booster Seats

### *A.1 Introduction*

The system used during the following test series is an earlier, less sophisticated version than what has been presented. The system used for this test series was only capable of using 3 measurement electrodes, in comparison to the current 6 measurement electrodes. The principles of operation between the two versions remain the same. There were also issues with the digital system microcontroller code used to calculate the X-Y-Z coordinates in real time. This led to the X-Y-Z displacements being calculated after each test rather than in real time. This was performed by attaching the data acquisition directly to the analog board outputs. This is an example of how the new system will be used in the future.

### *A.2 Methods*

Sled tests were conducted using a ServoSled (Seattle Safety, Seattle, WA) to recreate the Federal Motor Vehicle Safety Standard (FMVSS) 213 acceleration pulse specified in 49 Code of Federal Regulations Part 571 (Figure A.1) (49 US CFR Part 571.213).

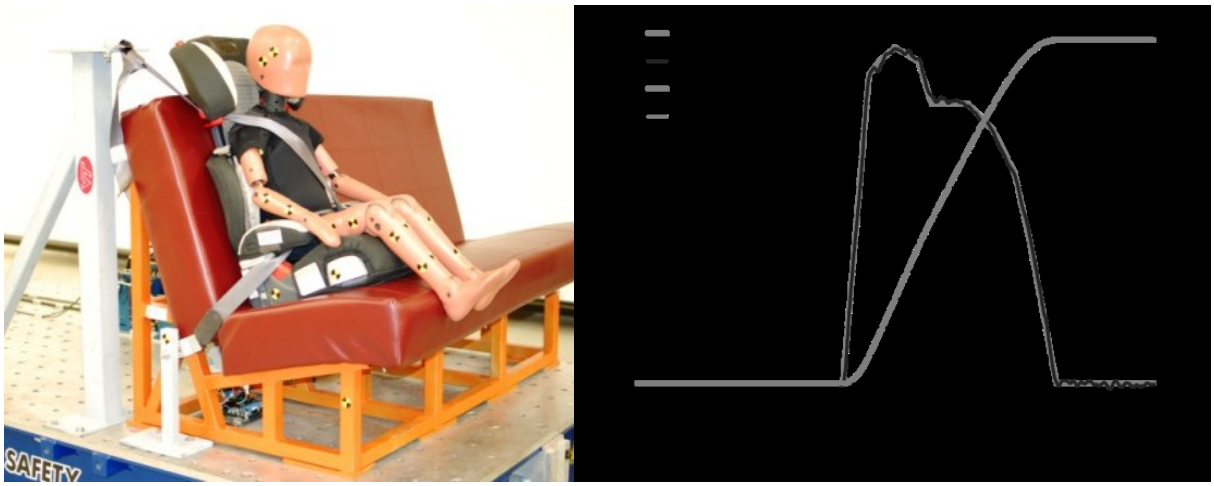


**Figure A.1:** Sled test configuration (left) and example sled pulse (right)

The regulatory and modified dummies were tested using two booster seats (Figure A.2), which will be henceforth referred to as SD1 and SD2, on an FMVSS 213 bench seat sled buck (non-standard foam). SD1 positioned the lap belt lower on the pelvis than SD2. There were 4 tests performed using each configuration, with a total of 16 tests performed overall. Belt positioning and dummy kinematics were compared visually using high speed video recorded at 1000 fps using three camera views (frontal, side, and oblique). This test series was conducted prior to the development of the six electrode abdomen, thus data was only collected from three superior measurement electrodes. Abdominal insert deflection measurements from the modified dummy tests were recorded using on-board data acquisition at 20 kHz.


**Figure A.2:** Booster seats used during the test series

*A.3 Visual Analysis*

The visual analysis from the high speed camera footage suggested a difference in the general kinematics of the regulatory dummy (Figure A.2) and the modified dummy (Figure A.4).

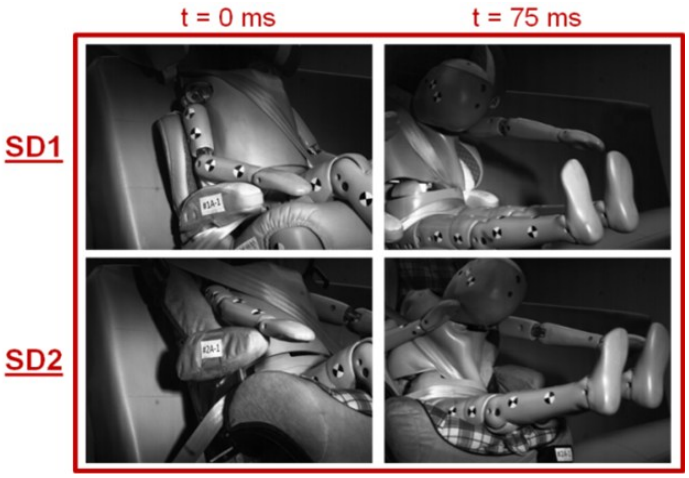


**Figure A.2:** Oblique camera view at 0 and 75ms for the regulatory dummy.

The regulatory dummy exhibited a mild case of submarining and similar overall kinematics for both seats. In some cases, entrapment of the belt in the abdominal cavity was observed. There were some cases in which the regulatory dummy experienced a more severe case of submarining in SD2 (Figure A.3), however these results were not consistent among all tests.

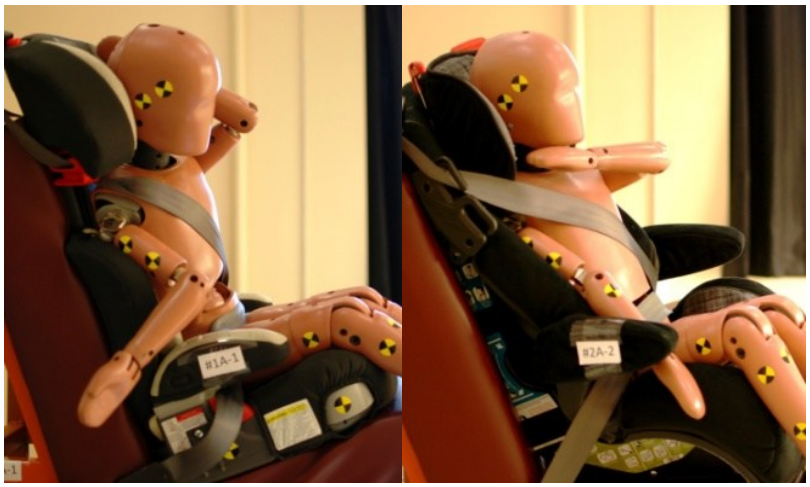

**Figure A.3:**SD1 (left) and SD2 (right) post-test belt placement for the regulatory dummy

The general kinematics of the modified dummy proved to be more reliable in differentiating between the two booster seats than the regulatory dummy (Figure A.4).

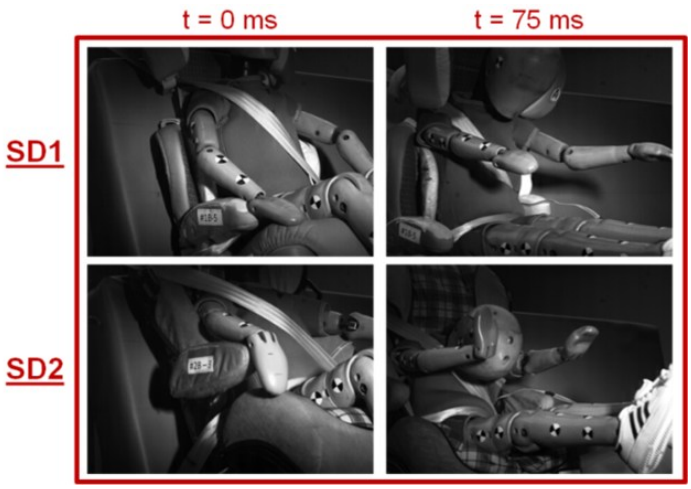


**Figure A.4:** Oblique camera view at 0 and 75ms for the modified dummy.

The modified dummy consistently exhibited a mild case of submarining in SD2. There was some slight roping of the belt in SD1; however the lap belt remained on the pelvis. Entrapment of the belt between the chest jacket and abdominal cavity was also observed in this case. Using the modified dummy, protrusion of the abdomen from the pelvis was present in both seats; however, superior outward displacement of the insert was more pronounced using SD2, which is indicative of a mild case of submarining in which the seatbelt interacts solely with the inferior ventral surface of the insert. This contributed to increased seatbelt-abdomen interaction as the dummy submarined.

The difference in overall kinematics is also observed through the comparison of the post-test seat belt placement in each booster seat for the modified dummy (Figure A.5).

**Figure A.5:**SD1 (left) and SD2 (right) post-test belt placement for the modified dummy

The difference in final belt placement is more clearly seen from a lateral view, where SD2 clearly shows higher belt placement than SD1, suggesting that only when the dummy was placed in SD2 did it experience a case of submarining. The roping of the lap belt on the pelvis is also more clearly visible in this view.

*A.4 Deflection Measurement Results*

Deflection measurement results are presented as X (P-A), Y (L-R), and Z (S-I) direction displacement of the individual electrodes relative to the dorsal reference electrode. The coordinate system was configured as per the Society of Automotive Engineers Recommended Practice J211. Each plot compares the average ± one standard deviation traces of the center superior ventral electrode displacement in the X (Figure A.6), Y, and Z directions (Figure A.7) for each of the four tests using SD1 and SD2. X displacement was initially positive, indicating that outward motion of the abdomen occurred in both seats, as noted from the high-speed video views. The average peak X displacement was measured to be 1.0 ± 3.4 mm and 31.2 ± 7.2 mm for SD1 and SD2 respectively (Table A.1). The difference in peak X displacement of SD1 compared to SD2 was found to be significant with a two-tailed t-test p-value of 0.0003.

Table A.1: Posterior-Anterior Abdomen Displacement

| | Mean Peak X (mm) | Std. Dev. | t-test p-value (as compared to other seat) |
|---|---|---|---|
| SD1 | 1.0 | 3.4 | 0.0003 |
| SD2 | 31.2 | 7.2 | 0.0003 |

Negative, or anterior to posterior, displacement was greater for SD2, matching the mild submarining observed visually for SD2 tests. Less than 5 mm of lateral (Y) displacement occurred and was slightly greater for SD2 compared to SD1. Z traces indicated upward motion for both seats.

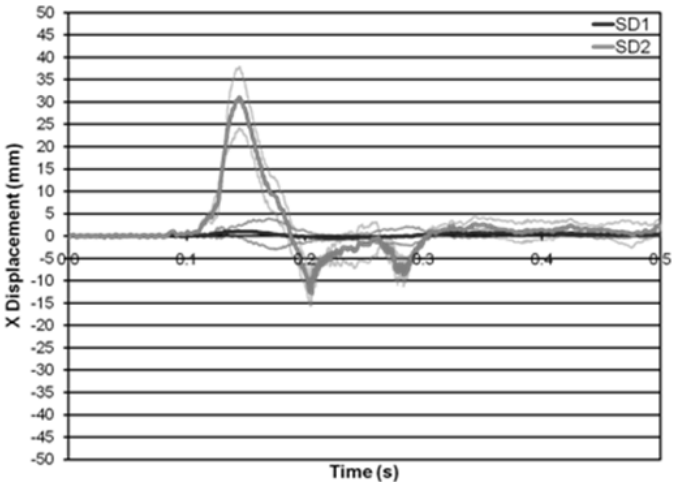


**Figure A.7:** Average deflection measurement for the center electrode in the X direction.

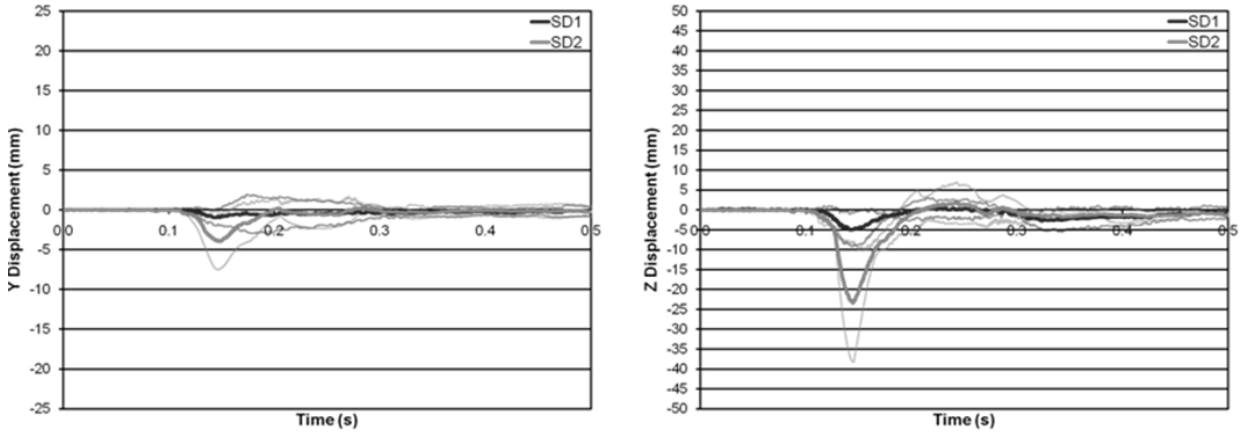


**Figure A.8:** Average deflection measurement for the center electrode in the Y and Z directions.

*A.5 System Integrity Test*

A single abdomen integrity sled test was conducted with the modified dummy seated in a pre-submarining position such that the lap belt directly loaded the abdomen at the onset of the test (Figure A.8). The pre-submarining condition allowed for a more severe case of submarining in which the lap belt loading a more superior aspect of the insert. This is indicated by the negative X displacement which shows an inward movement of the measurement electrode. The negative Z displacement also suggests the continued rotation of the dummy pelvis which would cause the measurement electrode to move superiorly as it was loaded in this condition.

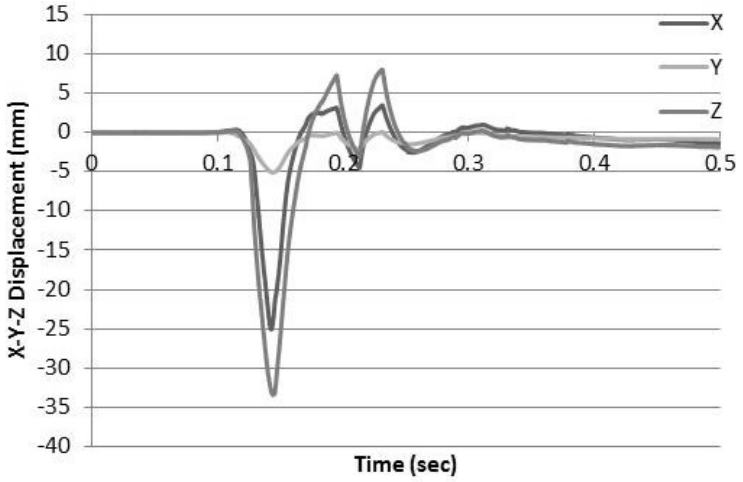


**Figure A.8:** X-Y-Z displacement of the central electrode in an abdomen integrity test.

*A.6 Discussion*

In general, the modified dummy was able to better distinguish between the SD1 and SD2 than the regulatory dummy. The data from the instrumented abdomen was consistent with the upward and outward motion of the abdomen due to belt loading of the lower aspects. The difference in peak X (P-A) displacement was found to be significant with a two-tailed t-test p value of 0.0003. The biofidelic abdomen and modified pelvis combination allow for improved ATD kinematics as compared to the regulatory dummy. This assessment of improvement is

based on the increased accuracy in anthropometry, scaled adult abdomen biomechanical response data, and comparison of the biofidelity with tests by Kent, et al. (2006).

The instrumented insert was shown to be robust and can withstand substantial penetration in the aforementioned integrity test. The pre-submarining condition allowed for the direct loading of the measurement electrodes during the entire acceleration pulse. The prior tests had loaded below the measurement electrodes, while this test allowed for direct compression of the abdomen insert and measurement electrodes.

The instrumented insert used for this test series contained only 3 measurement electrodes, instead of the current 6 measurement electrodes. The X-Y-Z trilateration calculations were performed post-test for this series. There were issues present with the microcontroller program used to perform the calculations. It is for this reason that the radius measurements from the analog board were sampled and output directly through the digital system in order to be interfaced with traditional data acquisition software. The version of the digital system used during this test series was also a scaled down version of the current configuration.

*A.7 Conclusion*

A practical deflection measurement system for the biofidelic abdominal insert was developed and implemented in the HIII 6-year-old dummy. The deflection measurement system was demonstrated for three dimensional quantification of abdominal insert deflection. The modified dummy with the instrumented insert discriminated between two different booster seat designs in FMVSS 213 sled tests, quantifying abdominal deflection due to belt interaction, and addressing a significant limitation of the current regulatory dummy.

Inclusion of the deflection measurement system into pediatric crash test dummies should lead to changes in frontal impact dummies geared toward improving child occupant safety.

Implementation of a 6-year-old abdominal insert with the ability to evaluate submarining potential should advance the effectiveness of booster seat design and restraint performance, leading to child occupant injury mitigation in automobile collisions.

*A.8 References*

49 US CFR Part 571.213: Child Restraint Systems & Part 572: Subpart I – Six-Year-Old Child.

Kent, R., Stacey, S., Kindig, M., Forman, J., Woods, W., Rouhana, SW., Higuchi, K., Tanji, H., Lawrence, SS., Arbogast, KB. Biomechanical Response of the Pediatric Abdomen, Part I: Development of an Experimental Model and Quantification of Structural Response to Dynamic Belt Loading. Stapp Car Crash J**50**.

**Appendix B: Microcontroller Source Code**

*B.1 Source Code "abdomenDigitalCode.c"*

```
/********************************************************************
 *
 *     PIC32MX Digital Board Code
 *
 ********************************************************************
 * FileName:       abdomenDigitalCode.c
 *
 * Dependencies:       p32xxxx.h
 *                                 plib.h
 *                                 stdlib.h
 *                                 math.h
 *                                 peripheral/spi.h
 *
 * Interrupts:             TMR1
 *                                 INT4
 *
 * Subfunctions:       systemInit
 *                                 stansqrt
 *
 * Processor:      PIC32MX
 *
 * Complier:       MPLAB C32
 *               MPLAB IDE
 *
 * Author:         T. Stan Gregory V
 *
 * Oscillator Configuration Bit Settings:
 *               - Oscillator Selection Bits =   Primary Osc w/PLL (XT+HS+EC+PLL)
 *               - Primary Oscillat5or Config =          HS osc mode
 *               - PLL Input Divider                     =       2x Divider
 *               - PLL Multiplier                        =       18x Multiplier
 *
 * Notes:
 *               - Set PBCLK divisor = 1:1 to achieve faster peripheral bus
 *               - Set Optimization Level to 3 (currently on s)
 *
********************************************************************/

// Dependencies
#include <p32xxxx.h>
#include <plib.h>
#include <stdlib.h>
#include <math.h>
```

```
#include <peripheral/spi.h>

/*********************************************************************/

// Configuration Bit settings

// SYSCLK = 80 MHz (8MHz Crystal/ FPLLIDIV * FPLLMUL / FPLLODIV)
#pragma config FPLLMUL = MUL_20, FPLLIDIV = DIV_2, FPLLODIV = DIV_1

// PBCLK = 80 MHz = SYSCLK / FPBDIV
// Primary Osc w/PLL (XT+,HS+,EC+PLL)
#pragma config POSCMOD = HS, FNOSC = PRIPLL, FPBDIV = DIV_1
#pragma config ICESEL = ICS_PGx2, DEBUG = OFF, CP=OFF, BWP=OFF, PWP=OFF,
IESO=OFF, OSCIOFNC = OFF

/*********************************************************************/

// Define System Frequency
#define SYS_FREQ                    (80000000L) //with 8MHz external oscillator

/*********************************************************************/

// Configure parallel port for operation with 16 bit data width
#define CONTROL             (PMP_ON | PMP_IDLE_CON | PMP_MUX_OFF |
PMP_READ_WRITE_OFF/* |\
            PMP_CS2_CS1_EN | PMP_LATCH_POL_HI | PMP_CS2_POL_LO |
PMP_CS1_POL_LO |\
            PMP_WRITE_POL_LO | PMP_READ_POL_LO)*/)

#define MODE        (PMP_IRQ_OFF | PMP_AUTO_ADDR_OFF | PMP_DATA_BUS_16 |
PMP_MODE_MASTER2 |\
            PMP_WAIT_BEG_1 | PMP_WAIT_MID_1 | PMP_WAIT_END_1 )

#define PORT      (PMP_PEN_OFF)

#define INTERRUPT   (PMP_INT_OFF)

/*********************************************************************/

// Define Variables
// long int  = 32 bit
// short int = 16 bit
// char     =  8 bit

// M Calibration Variables y=(x/m)+b
signed short int r1e0m=65;
```

```
signed short int r2e0m=367;
signed short int r3e0m=78;
signed short int r1e1m=61;
signed short int r2e1m=33;
signed short int r3e1m=33;
signed short int r1e2m=90;
signed short int r2e2m=41;
signed short int r3e2m=25;
signed short int r1e3m=45;
signed short int r2e3m=123;
signed short int r3e3m=60;
signed short int r1e4m=309;
signed short int r2e4m=-52;
signed short int r3e4m=103;
signed short int r1e5m=154;
signed short int r2e5m=123;
signed short int r3e5m=-104;
signed short int r1e6m=61;
signed short int r2e6m=103;
signed short int r3e6m=-104;

// B Calibration Variables y=(x/m)+b (Gets Recalculated)
signed short int r1e0b=38;
signed short int r2e0b=48;
signed short int r3e0b=537;
signed short int r1e1b=-238;
signed short int r2e1b=968;
signed short int r3e1b=1262;
signed short int r1e2b=2;
signed short int r2e2b=-66;
signed short int r3e2b=370;
signed short int r1e3b=-121;
signed short int r2e3b=100;
signed short int r3e3b=-7;
signed short int r1e4b=73;
signed short int r2e4b=681;
signed short int r3e4b=297;
signed short int r1e5b=166;
signed short int r2e5b=282;
signed short int r3e5b=412;
signed short int r1e6b=60;
signed short int r2e6b=628;
signed short int r3e6b=1738;

// Initial Position Radius Values (mm)
signed short int r1e0i=39;      //38.5;
```

```
signed short int r2e0i=39;      //38.5;
signed short int r3e0i=53;      //53.3;
signed short int r1e1i=96;      //95.6;
signed short int r2e1i=74;      //74.1;
signed short int r3e1i=94;      //94.3;
signed short int r1e2i=76;      //76.4;
signed short int r2e2i=77;      //76.5;
signed short int r3e2i=86;      //85.6;
signed short int r1e3i=75;      //74.5;
signed short int r2e3i=98;      //98.3;
signed short int r3e3i=96;      //95.5;
signed short int r1e4i=70;      //70.0;
signed short int r2e4i=56;      //56.2;
signed short int r3e4i=64;      //63.7;
signed short int r1e5i=56;      //56.0;
signed short int r2e5i=72;      //71.8;
signed short int r3e5i=65;      //64.5;
signed short int r1e6i=58;      //57.7;
signed short int r2e6i=58;      //58.1;
signed short int r3e6i=52;      //51.6;

// Raw ADC Sampled Data
signed short int r1e0=0;
signed short int r2e0=0;
signed short int r3e0=0;
signed short int r1e1=0;
signed short int r2e1=0;
signed short int r3e1=0;
signed short int r1e2=0;
signed short int r2e2=0;
signed short int r3e2=0;
signed short int r1e3=0;
signed short int r2e3=0;
signed short int r3e3=0;
signed short int r1e4=0;
signed short int r2e4=0;
signed short int r3e4=0;
signed short int r1e5=0;
signed short int r2e5=0;
signed short int r3e5=0;
signed short int r1e6=0;
signed short int r2e6=0;
signed short int r3e6=0;

// Calibrated & Squared ADC Data
signed long int sr1e0=0;
```

```
signed long int sr2e0=0;
signed long int sr3e0=0;
signed long int sr1e1=0;
signed long int sr2e1=0;
signed long int sr3e1=0;
signed long int sr1e2=0;
signed long int sr2e2=0;
signed long int sr3e2=0;
signed long int sr1e3=0;
signed long int sr2e3=0;
signed long int sr3e3=0;
signed long int sr1e4=0;
signed long int sr2e4=0;
signed long int sr3e4=0;
signed long int sr1e5=0;
signed long int sr2e5=0;
signed long int sr3e5=0;
signed long int sr1e6=0;
signed long int sr2e6=0;
signed long int sr3e6=0;

// XYZ Calculations
signed short int xse0=0;
signed long int x2e0=0;
signed short int yse0=0;
signed long int y2e0=0;
signed short int zse0=0;
signed long int z2e0=0;
signed short int xse1=0;
signed long int x2e1=0;
signed short int yse1=0;
signed long int y2e1=0;
signed short int zse1=0;
signed long int z2e1=0;
signed short int xse2=0;
signed long int x2e2=0;
signed short int yse2=0;
signed long int y2e2=0;
signed short int zse2=0;
signed long int z2e2=0;
signed short int xse3=0;
signed long int x2e3=0;
signed short int yse3=0;
signed long int y2e3=0;
signed short int zse3=0;
signed long int z2e3=0;
```

```
signed short int xse4=0;
signed long int x2e4=0;
signed short int yse4=0;
signed long int y2e4=0;
signed short int zse4=0;
signed long int z2e4=0;
signed short int xse5=0;
signed long int x2e5=0;
signed short int yse5=0;
signed long int y2e5=0;
signed short int zse5=0;
signed long int z2e5=0;
signed short int xse6=0;
signed long int x2e6=0;
signed short int yse6=0;
signed long int y2e6=0;
signed short int zse6=0;
signed long int z2e6=0;

// Rotation Variables
signed short int xrre0=0;
signed short int yrre0=0;
signed short int zrre0=0;
signed short int xrre1=0;
signed short int yrre1=0;
signed short int zrre1=0;
signed short int xrre2=0;
signed short int yrre2=0;
signed short int zrre2=0;
signed short int xrre3=0;
signed short int yrre3=0;
signed short int zrre3=0;
signed short int xrre4=0;
signed short int yrre4=0;
signed short int zrre4=0;
signed short int xrre5=0;
signed short int yrre5=0;
signed short int zrre5=0;
signed short int xrre6=0;
signed short int yrre6=0;
signed short int zrre6=0;

// Final XYZ Data (After Ref is accounted for)
unsigned long int xf0=0;
unsigned long int yf0=0;
unsigned long int zf0=0;
```

```
unsigned long int xf1=0;
unsigned long int yf1=0;
unsigned long int zf1=0;
unsigned long int xf2=0;
unsigned long int yf2=0;
unsigned long int zf2=0;
unsigned long int xf3=0;
unsigned long int yf3=0;
unsigned long int zf3=0;
unsigned long int xf4=0;
unsigned long int yf4=0;
unsigned long int zf4=0;
unsigned long int xf5=0;
unsigned long int yf5=0;
unsigned long int zf5=0;
unsigned long int xf6=0;
unsigned long int yf6=0;
unsigned long int zf6=0;

// Values to Add DAC Offset to XYZ data
signed long int xf1o=32760;
signed long int yf1o=32760;
signed long int zf1o=32760;
signed long int xf2o=32760;
signed long int yf2o=32760;
signed long int zf2o=32760;
signed long int xf3o=32760;
signed long int yf3o=32760;
signed long int zf3o=32760;
signed long int xf4o=32760;
signed long int yf4o=32760;
signed long int zf4o=32760;
signed long int xf5o=32760;
signed long int yf5o=32760;
signed long int zf5o=32760;
signed long int xf6o=32760;
signed long int yf6o=32760;
signed long int zf6o=32760;

// Ref Electrode
signed long int refx=0;
signed long int refy=0;
signed long int refz=0;

// Initial Ref Electrode Position
signed short int refx0=0;
```

```
signed short int refy0=0;
signed short int refz0=0;

// Misc Variables
unsigned long int ii=0; // ADC Software Reset Counter
unsigned long int jj=0; // Take Initial Values and Solve for b (y=x/m+b)

/*********************************************************************/

// Define Pins
// ADC
#define CONVST              IOPORT_G, BIT_6
#define RESET               IOPORT_C, BIT_4
#define BUSY          IOPORT_C, BIT_2

#define RDCS1               IOPORT_D, BIT_3
#define RDCS2               IOPORT_C, BIT_1
#define RDCS3               IOPORT_C, BIT_3

// DAC
#define SYNC1               IOPORT_E, BIT_8
#define SYNC2               IOPORT_E, BIT_9
#define SYNC3               IOPORT_B, BIT_5
#define SYNC4               IOPORT_B, BIT_4
#define SYNC5               IOPORT_B, BIT_3

// Misc
#define LED1          IOPORT_B, BIT_6
#define TOGG                IOPORT_D, BIT_0

/*********************************************************************/

// System Initialization
void systemInit(void){

        // Preset Pin Conditions
        PORTSetBits(SYNC1);
        PORTSetBits(SYNC2);
        PORTSetBits(SYNC3);
        PORTSetBits(SYNC4);
        PORTSetBits(SYNC5);

        PORTSetBits(CONVST);
        PORTSetBits(RDCS1);
        PORTSetBits(RDCS2);
        PORTSetBits(RDCS3);
```

```
	PORTClearBits(RESET);

	// Turn on LED
	PORTSetBits(LED1);

	// Wait for ADC Boot-up
	while(ii<400){
		asm("nop");
		ii++;
	}
	ii=0;

	// ADC Software Reset
	PORTSetBits(RESET);
	while(ii<5){
		asm("nop");
		ii++;
	}
	ii=0;
	PORTClearBits(RESET);
}

/*********************************************************************/

int main(void)
{

	//Hardware Configure
	SYSTEMConfig(SYS_FREQ,  SYS_CFG_WAIT_STATES  |  SYS_CFG_PCACHE);  //
Configure cache, wait states and peripheral bus clock
	SYSTEMConfigPerformance(SYS_FREQ);

	// I/O Configure
	PORTSetPinsDigitalOut(IOPORT_G, BIT_6);
	PORTSetPinsDigitalOut(IOPORT_E, BIT_8 | BIT_9);
	PORTSetPinsDigitalOut(IOPORT_D, BIT_3 | BIT_0);
	PORTSetPinsDigitalOut(IOPORT_C, BIT_4 | BIT_3 | BIT_1);
	PORTSetPinsDigitalOut(IOPORT_B, BIT_5 | BIT_4 | BIT_3 | BIT_6);
	PORTSetPinsDigitalOut(IOPORT_A, BIT_0 | BIT_14);

	PORTSetPinsDigitalIn(IOPORT_C, BIT_2);
	PORTSetPinsDigitalIn(IOPORT_A, BIT_15);

	// System Setup
	mPMPOpen(CONTROL, MODE, PORT, INTERRUPT);
	systemInit();
```

```
        // Timer1 & Interrupt Setup
   OpenTimer1(T1_ON | T1_SOURCE_INT | T1_PS_1_1, 5000); // Configure Timer 1 using
internal clock --> 20kHz
   ConfigIntTimer1(T1_INT_ON | T1_INT_PRIOR_1);              // set up the timer interrupt
with a priority of 1
   //ConfigINT4(EXT_INT_PRI_7|RISING_EDGE_INT|EXT_INT_ENABLE);   //   External
Button Press Interrupt
        INTEnableSystemMultiVectoredInt();                                  // enable multi-vector
interrupts

        // SPI Configure
        SpiChnOpen(1,   SPI_OPEN_MODE32|SPI_OPEN_MSTEN|SPI_OPEN_SMP_END,4);
        //Open Channel 1, Master, 32bit width, Fosc/4
        SPI1BRG=0;
                                // Set FSCK to Fosc/2

        // While Loop
   while(1){
                // Do Nothing
        }

}

/*********************************************************************/

// Timer 1 Interrupt
void __ISR(_TIMER_1_VECTOR, ipl2) _Timer1Handler(void)
{
   // Clear the Interrupt Flag
   mT1ClearIntFlag();

        // Toggle Pin
        PORTToggleBits(TOGG);

        // Set Master Address
        PMADDR = 0x4000;

        // Retrieve ADC Data
                PORTToggleBits(SYNC1);
                SPI1BUF=(xf1)*16+50331648;   // X1 DAC 1A

                PORTToggleBits(RDCS1);
                r1e1=PMDIN;
                r1e1=PMDIN;
                r1e1=PMDIN;
```

```
PORTToggleBits(RDCS1);
PORTToggleBits(RDCS1);
r2e1=PMDIN;
r2e1=PMDIN;
r2e1=PMDIN;
PORTToggleBits(RDCS1);

PORTToggleBits(SYNC1);
PORTToggleBits(SYNC2);
SPI1BUF=(yf1)*16+52428800;   // Y1 DAC 2C

PORTToggleBits(RDCS1);
r3e1=PMDIN;
r3e1=PMDIN;
r3e1=PMDIN;
PORTToggleBits(RDCS1);
PORTToggleBits(RDCS1);
r1e2=PMDIN;
r1e2=PMDIN;
r1e2=PMDIN;
PORTToggleBits(RDCS1);

PORTToggleBits(SYNC2);
PORTToggleBits(SYNC4);
SPI1BUF=(zf1)*16+50331648;   // Z1 DAC 4A

PORTToggleBits(RDCS1);
r2e2=PMDIN;
r2e2=PMDIN;
r2e2=PMDIN;
PORTToggleBits(RDCS1);
PORTToggleBits(RDCS1);
r3e2=PMDIN;
r3e2=PMDIN;
r3e2=PMDIN;
PORTToggleBits(RDCS1);

PORTToggleBits(SYNC4);
PORTToggleBits(SYNC1);
SPI1BUF=(xf2)*16+51380224;   // X2 DAC 1B

PORTToggleBits(RDCS1);
r1e4=PMDIN;
r1e4=PMDIN;
r1e4=PMDIN;
PORTToggleBits(RDCS1);
```

```
PORTToggleBits(RDCS1);
r2e4=PMDIN;
r2e4=PMDIN;
r2e4=PMDIN;
PORTToggleBits(RDCS1);

PORTToggleBits(SYNC1);
PORTToggleBits(SYNC2);
SPI1BUF=(yf2)*16+53477376;   // Y2 DAC 2D

PORTToggleBits(RDCS2);
r3e4=PMDIN;
r3e4=PMDIN;
r3e4=PMDIN;
PORTToggleBits(RDCS2);
PORTToggleBits(RDCS2);
r1e5=PMDIN;
r1e5=PMDIN;
r1e5=PMDIN;
PORTToggleBits(RDCS2);

PORTToggleBits(SYNC2);
PORTToggleBits(SYNC4);
SPI1BUF=(zf2)*16+51380224;   // Z2 DAC 4B

PORTToggleBits(RDCS2);
r2e5=PMDIN;
r2e5=PMDIN;
r2e5=PMDIN;
PORTToggleBits(RDCS2);
PORTToggleBits(RDCS2);
r3e5=PMDIN;
r3e5=PMDIN;
r3e5=PMDIN;
PORTToggleBits(RDCS2);

PORTToggleBits(SYNC4);
PORTToggleBits(SYNC1);
SPI1BUF=(xf3)*16+52428800;   // X3 DAC 1C

PORTToggleBits(RDCS2);
r1e3=PMDIN;
r1e3=PMDIN;
r1e3=PMDIN;
PORTToggleBits(RDCS2);
PORTToggleBits(RDCS2);
```

```
r2e3=PMDIN;
r2e3=PMDIN;
r2e3=PMDIN;
PORTToggleBits(RDCS2);

PORTToggleBits(SYNC1);
PORTToggleBits(SYNC3);
SPI1BUF=(yf3)*16+50331648;   // Y3 DAC 3A

PORTToggleBits(RDCS2);
r3e3=PMDIN;
r3e3=PMDIN;
r3e3=PMDIN;
PORTToggleBits(RDCS2);
PORTToggleBits(RDCS2);
r1e0=PMDIN;
r1e0=PMDIN;
r1e0=PMDIN;
PORTToggleBits(RDCS2);

PORTToggleBits(SYNC3);
PORTToggleBits(SYNC4);
SPI1BUF=(zf3)*16+52428800;   // Z3 DAC 4C

PORTToggleBits(RDCS3);
r2e0=PMDIN;
r2e0=PMDIN;
r2e0=PMDIN;
PORTToggleBits(RDCS3);
PORTToggleBits(RDCS3);
r3e0=PMDIN;
r3e0=PMDIN;
r3e0=PMDIN;
PORTToggleBits(RDCS3);

PORTToggleBits(SYNC4);
PORTToggleBits(SYNC1);
SPI1BUF=(xf4)*16+53477376;   // X4 DAC 1D

PORTToggleBits(RDCS3);
r1e6=PMDIN;
r1e6=PMDIN;
r1e6=PMDIN;
PORTToggleBits(RDCS3);
PORTToggleBits(RDCS3);
r2e6=PMDIN;
```

```
        r2e6=PMDIN;
        r2e6=PMDIN;
        PORTToggleBits(RDCS3);

        PORTToggleBits(SYNC1);
        PORTToggleBits(SYNC3);
        SPI1BUF=(yf4)*16+51380224;   // Y4 DAC 3B

        PORTToggleBits(RDCS3);
        r3e6=PMDIN;
        r3e6=PMDIN;
        r3e6=PMDIN;
        PORTToggleBits(RDCS3);

// ADC Conversion (Read During Conversion, no BUSY)
PORTClearBits(CONVST);
PORTSetBits(CONVST);

// Reference Electrode
        // Calibrate Data
        r1e0=r1e0/r1e0m+r1e0b;
        r2e0=r2e0/r2e0m+r2e0b;
        r3e0=r3e0/r3e0m+r3e0b;

        PORTToggleBits(SYNC3);
        PORTToggleBits(SYNC4);
        SPI1BUF=(zf4)*16+53477376;   // Z4 DAC 4D

        // Square Data
        sr1e0=r1e0*r1e0; // 16 bit square
        sr2e0=r2e0*r2e0;
        sr3e0=r3e0*r3e0;

        // Apply Gain
        sr1e0=sr1e0*10;
        sr2e0=sr2e0*10;
        sr3e0=sr3e0*10;

        // XYZ Calculation
        xse0=(sr1e0-sr2e0)/76+190;
        yse0=(sr1e0-sr3e0)/38+190-xse0;
        x2e0=xse0;
        x2e0=x2e0*x2e0;
        y2e0=yse0;
        y2e0=y2e0*y2e0;
        z2e0=stansqrt(abs(sr1e0-(y2e0)-(x2e0)));
```

```
        zse0=z2e0;

        PORTToggleBits(SYNC4);
        PORTToggleBits(SYNC2);
        SPI1BUF=(xf5)*16+50331648;   // X5 DAC 2A

        // Apply Rotation Matrices
        y2e0=zse0;
        z2e0=yse0;

        y2e0=10*y2e0;
        z2e0=-10*z2e0;

        refx=(y2e0/11)-(z2e0/29)-25;
        refy=xse0-19;
        refz=25-(y2e0/29)-(z2e0/11);

        // Account for Initial Position
        refx=refx-refx0;
        refy=refy-refy0;
        refz=refz-refz0;

        // Null Values for Debugging
        /*refx=0;
        refy=0;
        refz=0;*/

// Electrode 1
        // Calibrate Data
        r1e1=r1e1/r1e1m+r1e1b;
        r2e1=r2e1/r2e1m+r2e1b;
        r3e1=r3e1/r3e1m+r3e1b;

        PORTToggleBits(SYNC2);
        PORTToggleBits(SYNC3);
        SPI1BUF=(yf5)*16+52428800;   // Y5 DAC 3C

        // Square Data
        sr1e1=r1e1*r1e1; // 16 bit square
        sr2e1=r2e1*r2e1;
        sr3e1=r3e1*r3e1;

        // Apply Gain
        sr1e1=sr1e1*10;
        sr2e1=sr2e1*10;
        sr3e1=sr3e1*10;
```

```
        // XYZ Calculation
        xse1=(sr1e1-sr2e1)/76+190;
        yse1=(sr1e1-sr3e1)/38+190-xse1;
        x2e1=xse1;
        x2e1=x2e1*x2e1;
        y2e1=yse1;
        y2e1=y2e1*y2e1;
        z2e1=stansqrt(abs(sr1e1-(y2e1)-(x2e1)));
        zse1=z2e1;

        PORTToggleBits(SYNC3);
        PORTToggleBits(SYNC5);
        SPI1BUF=(zf5)*16+50331648;   // Z5 DAC 5A

        // Apply Rotation Matrices // This was saving numbers to y2e1 and z2e1
        y2e1=zse1;
        z2e1=yse1;

        z2e1=-10*z2e1;
        y2e1=10*y2e1;

        xrre1=(y2e1/11)-(z2e1/29)+250;
        yrre1=xse1;
        zrre1=250-(y2e1/29)-(z2e1/11);

        // Account for Reference Electrode
        xrre1=xrre1-refx;
        yrre1=yrre1-refy;
        zrre1=zrre1-refz;

        // Add Offset
        xf1=(xrre1+xf1o);
        yf1=(yrre1+yf1o);
        zf1=(zrre1+zf1o);

// Electrode 2
        // Calibrate Data
        r1e2=r1e2/r1e2m+r1e2b;
        r2e2=r2e2/r2e2m+r2e2b;
        r3e2=r3e2/r3e2m+r3e2b;

        PORTToggleBits(SYNC5);
        PORTToggleBits(SYNC2);
        SPI1BUF=(xf6)*16+51380224;   // X6 DAC 2B
```

```
        // Square Data
        sr1e2=r1e2*r1e2; // 16 bit square
        sr2e2=r2e2*r2e2;
        sr3e2=r3e2*r3e2;

        // Apply Gain
        sr1e2=sr1e2*10;
        sr2e2=sr2e2*10;
        sr3e2=sr3e2*10;

        // XYZ Calculation
        xse2=(sr1e2-sr2e2)/76+190;
        yse2=(sr1e2-sr3e2)/38+190-xse2;
        x2e2=xse2;
        x2e2=x2e2*x2e2;
        y2e2=yse2;
        y2e2=y2e2*y2e2;
        z2e2=stansqrt(abs(sr1e2-(y2e2)-(x2e2)));
        zse2=z2e2;

        PORTToggleBits(SYNC2);
        PORTToggleBits(SYNC3);
        SPI1BUF=(yf6)*16+53477376;   // Y6 DAC 3D

        // Apply Rotation Matrices
        y2e2=zse2;
        z2e2=yse2;

        z2e2=z2e2*-10;
        y2e2=y2e2*10;

        xrre2=(y2e2/11)-(z2e2/29)+250;
        yrre2=xse2;
        zrre2=-250-(y2e2/29)-(z2e2/11);

        // Account for Reference Electrode
        xrre2=xrre2-refx;
        yrre2=yrre2-refy;
        zrre2=zrre2-refz;

        // Add Offset
        xf2=(xrre2+xf2o);
        yf2=(yrre2+yf2o);
        zf2=(zrre2+zf2o);

// Electrode 3
```

```
// Calibrate Data
r1e3=r1e3/r1e3m+r1e3b;
r2e3=r2e3/r2e3m+r2e3b;
r3e3=r3e3/r3e3m+r3e3b;

PORTToggleBits(SYNC3);
PORTToggleBits(SYNC5);
SPI1BUF=(zf6)*16+52428800;   // Z6 DAC 5C

// Square Data
sr1e3=r1e3*r1e3; // 16 bit square
sr2e3=r2e3*r2e3;
sr3e3=r3e3*r3e3;

// Apply Gain
sr1e3=sr1e3*10;
sr2e3=sr2e3*10;
sr3e3=sr3e3*10;

// XYZ Calculation
xse3=(sr1e3-sr2e3)/76+190;
yse3=(sr1e3-sr3e3)/38+190-xse3;
x2e3=xse3;
x2e3=x2e3*x2e3;
y2e3=yse3;
y2e3=y2e3*y2e3;
z2e3=stansqrt(abs(sr1e3-(y2e3)-(x2e3)));
zse3=z2e3;

PORTToggleBits(SYNC5);

// Apply Rotation Matrices
y2e3=zse3;
z2e3=yse3;

z2e3=-10*z2e3;
y2e3=10*y2e3;

xrre3=(y2e3/11)-(z2e3/29)+250;
yrre3=xse3;
zrre3=250-(y2e3/29)-(z2e3/11);

// Account for Reference Electrode
xrre3=xrre3-refx;
yrre3=yrre3-refy;
zrre3=zrre3-refz;
```

```
        // Add Offset
        xf3=(xrre3+xf3o);
        yf3=(yrre3+yf3o);
        zf3=(zrre3+zf3o);

// Electrode 4
        // Calibrate Data
        r1e4=r1e4/r1e4m+r1e4b;
        r2e4=r2e4/r2e4m+r2e4b;
        r3e4=r3e4/r3e4m+r3e4b;

        // Square Data
        sr1e4=r1e4*r1e4; // 16 bit square
        sr2e4=r2e4*r2e4;
        sr3e4=r3e4*r3e4;

        // Apply Gain
        sr1e4=sr1e4*10;
        sr2e4=sr2e4*10;
        sr3e4=sr3e4*10;

        // XYZ Calculation
        xse4=(sr1e4-sr2e4)/76+190;
        yse4=(sr1e4-sr3e4)/38+190-xse4;
        x2e4=xse4;
        x2e4=x2e4*x2e4;
        y2e4=yse4;
        y2e4=y2e4*y2e4;
        z2e4=stansqrt(abs(sr1e4-(y2e4)-(x2e4)));
        zse4=z2e4;


        // Apply Rotation Matrices
        y2e4=zse4;
        z2e4=yse4;

        z2e4=-10*z2e4;
        y2e4=10*y2e4;

        xrre4=(y2e4/11)-(z2e4/29)+250;
        yrre4=xse4;
        zrre4=250-(y2e4/29)-(z2e4/11);

        // Account for Reference Electrode
        xrre4=xrre4-refx;
```

```
        yrre4=yrre4-refy;
        zrre4=zrre4-refz;

        // Add Offset
        xf4=(xrre4+xf4o);
        yf4=(yrre4+yf4o);
        zf4=(zrre4+zf4o);

// Electrode 5
        // Calibrate Data
        r1e5=r1e5/r1e5m+r1e5b;
        r2e5=r2e5/r2e5m+r2e5b;
        r3e5=r3e5/r3e5m+r3e5b;

        // Square Data
        sr1e5=r1e5*r1e5; // 16 bit square
        sr2e5=r2e5*r2e5;
        sr3e5=r3e5*r3e5;

        // Apply Gain
        sr1e5=sr1e5*10;
        sr2e5=sr2e5*10;
        sr3e5=sr3e5*10;

        // XYZ Calculation
        xse5=(sr1e5-sr2e5)/76+190;
        yse5=(sr1e5-sr3e5)/38+190-xse5;
        x2e5=xse5;
        x2e5=x2e5*x2e5;
        y2e5=yse5;
        y2e5=y2e5*y2e5;
        z2e5=stansqrt(abs(sr1e5-(y2e5)-(x2e5)));
        zse5=z2e5;


        // Apply Rotation Matrices
        y2e5=zse5;
        z2e5=yse5;

        z2e5=-10*z2e5;
        y2e5=10*y2e5;

        xrre5=(y2e5/11)-(z2e5/29)+250;
        yrre5=xse5;
        zrre5=250-(y2e5/29)-(z2e5/11);
```

```
        // Account for Reference Electrode
        xrre5=xrre5-refx;
        yrre5=yrre5-refy;
        zrre5=zrre5-refz;

        // Add Offset
        xf5=(xrre5+xf5o);
        yf5=(yrre5+yf5o);
        zf5=(zrre5+zf5o);

// Electrode 6
        // Calibrate Data
        r1e6=r1e6/r1e6m+r1e6b;
        r2e6=r2e6/r2e6m+r2e6b;
        r3e6=r3e6/r3e6m+r3e6b;

        // Square Data
        sr1e6=r1e6*r1e6; // 16 bit square
        sr2e6=r2e6*r2e6;
        sr3e6=r3e6*r3e6;

        // Apply Gain
        sr1e6=sr1e6*10;
        sr2e6=sr2e6*10;
        sr3e6=sr3e6*10;

        // XYZ Calculation
        xse6=(sr1e6-sr2e6)/76+190;
        yse6=(sr1e6-sr3e6)/38+190-xse6;
        x2e6=xse6;
        x2e6=x2e6*x2e6;
        y2e6=yse6;
        y2e6=y2e6*y2e6;
        z2e6=stansqrt(abs(sr1e6-(y2e6)-(x2e6)));
        zse6=z2e6;


        // Apply Rotation Matrices
        y2e6=zse6;
        z2e6=yse6;

        z2e6=-10*z2e6;
        y2e6=10*y2e6;

        xrre6=(y2e6/11)-(z2e6/29)+250;
        yrre6=xse6;
```

```
zrre6=250-(y2e6/29)-(z2e6/11);

// Account for Reference Electrode
xrre6=xrre6-refx;
yrre6=yrre6-refy;
zrre6=zrre6-refz;

// Add Offset
xf6=(xrre6+xf6o);
yf6=(yrre6+yf6o);
zf6=(zrre6+zf6o);

// Solve for B on Initial Run
if (jj==20000){
        PORTClearBits(LED1);
        r1e0b=r1e0i-(r1e0/r1e0m);
        r2e0b=r2e0i-(r2e0/r2e0m);
        r3e0b=r3e0i-(r3e0/r3e0m);

        r1e1b=r1e1i-(r1e1/r1e1m);
        r2e1b=r2e1i-(r2e1/r2e1m);
        r3e1b=r3e1i-(r3e1/r3e1m);

        r1e2b=r1e2i-(r1e2/r1e2m);
        r2e2b=r2e2i-(r2e2/r2e2m);
        r3e2b=r3e2i-(r3e2/r3e2m);

        r1e3b=r1e3i-(r1e3/r1e3m);
        r2e3b=r2e3i-(r2e3/r2e3m);
        r3e3b=r3e3i-(r3e3/r3e3m);

        r1e4b=r1e4i-(r1e4/r1e4m);
        r2e4b=r2e4i-(r2e4/r2e4m);
        r3e4b=r3e4i-(r3e4/r3e4m);

        r1e5b=r1e5i-(r1e5/r1e5m);
        r2e5b=r2e5i-(r2e5/r2e5m);
        r3e5b=r3e5i-(r3e5/r3e5m);

        r1e6b=r1e6i-(r1e6/r1e6m);
        r2e6b=r2e6i-(r2e6/r2e6m);
        r3e6b=r3e6i-(r3e6/r3e6m);
}

if (jj==30000){
        xf1o=32760-xrre1;
```

```
                    yf1o=32760-yrre1;
                    zf1o=32760-zrre1;

                    xf2o=32760-xrre2;
                    yf2o=32760-yrre2;
                    zf2o=32760-zrre2;

                    xf3o=32760-xrre3;
                    yf3o=32760-yrre3;
                    zf3o=32760-zrre3;

                    xf4o=32760-xrre4;
                    yf4o=32760-yrre4;
                    zf4o=32760-zrre4;

                    xf5o=32760-xrre5;
                    yf5o=32760-yrre5;
                    zf5o=32760-zrre5;

                    xf6o=32760-xrre6;
                    yf6o=32760-yrre6;
                    zf6o=32760-zrre6;

                    PORTSetBits(LED1);
                }

                if (jj<35000){jj=jj+1;}

} // End Timer 1

/*********************************************************************/

// Square Root Function

int stansqrt(num)
{
   int op = num;
   int res = 0;
   int one = 1 << 30;

   while (one > op)
      one >>= 2;

   while (one != 0) {
      if (op >= res + one) {
         op -= res + one;
```

```
            res = (res >> 1) + one;
        }
        else
          res >>= 1;
        one >>= 2;
    }
    return res;
}

/*****************************************************************************
```